Title

Tau covariance patterns in Alzheimer's disease patients match intrinsic connectivity networks in the healthy brain

Authors

Ossenkoppele, Rik
Iaccarino, Leonardo
Schonhaut, Daniel R
et al.

Publication Date

2019

DOI

10.1016/j.nicl.2019.101848

Peer reviewed

NeuroImage: Clinical 23 (2019) 101848

Contents lists available at ScienceDirect

NeuroImage: Clinical

journal homepage: www.elsevier.com/locate/ynicl

Tau covariance patterns in Alzheimer's disease patients match intrinsic connectivity networks in the healthy brain

Rik Ossenkoppele[a,b,c,*], Leonardo Iaccarino[a], Daniel R. Schonhaut[a,b], Jesse A. Brown[a], Renaud La Joie[a,b], James P. O'Neil[d], Mustafa Janabi[d], Suzanne L. Baker[d], Joel H. Kramer[a], Maria-Luisa Gorno-Tempini[a], Bruce L. Miller[a], Howard J. Rosen[a], William W. Seeley[a,e], William J. Jagust[b,d], Gil D. Rabinovici[a,b]

[a] Memory and Aging Center, University of California San Francisco, San Francisco, CA 94143, USA
[b] Helen Wills Neuroscience Institute, University of California Berkeley, Berkeley, CA 94720, USA
[c] Department of Neurology & Alzheimer Center, Neuroscience Campus Amsterdam, VU University Medical Center, Amsterdam 1081 HZ, the Netherlands
[d] Molecular Biophysics and Integrated Bioimaging Division, Lawrence Berkeley National Laboratory, Berkeley, CA 94720, USA
[e] Department of Pathology, University of California San Francisco, San Francisco, CA 94143, USA

ARTICLE INFO

Keywords:
Alzheimer's disease
Flortaucipir
Functional connectivity
PET
Tau
Amyloid

ABSTRACT

According to the network model of neurodegeneration, the spread of pathogenic proteins occurs selectively along connected brain regions. We tested in vivo whether the distribution of filamentous tau (measured with [^{18}F]flortaucipir-PET), fibrillar amyloid-β ([^{11}C]PIB-PET) and glucose hypometabolism ([^{18}F]FDG-PET) follows the intrinsic functional organization of the healthy brain. We included 63 patients with Alzheimer's disease (AD; 30 male, 63 ± 8 years) who underwent [^{18}F]flortaucipir, [^{11}C]PIB and [^{18}F]FDG PET, and 1000 young adults (427 male, 21 ± 3 years) who underwent task-free fMRI. We selected six predefined disease epicenters as seeds for whole-brain voxelwise covariance analyses to compare correlated patterns of tracer uptake across AD patients against fMRI intrinsic connectivity patterns in young adults. We found a striking convergence between [^{18}F]flortaucipir covariance patterns and intrinsic connectivity maps (range Spearman rho's: 0.32–0.78, $p < .001$), which corresponded with expected functional networks (range goodness-of-fit: 3.8–8.2). The topography of amyloid-β covariance patterns was more diffuse and less network-specific, while glucose hypometabolic patterns were more spatially restricted than tau but overlapped with functional networks. These findings suggest that the spatial patterns of tau and glucose hypometabolism observed in AD resemble the functional organization of the healthy brain, supporting the notion that tau pathology spreads through circumscribed brain networks and drives neurodegeneration.

1. Introduction

Neuropathological, cell culture and animal studies have shown that Alzheimer's disease (AD) hallmark proteins amyloid-β (Aβ) and tau, and pathogenic proteins in other neurodegenerative conditions, do not spread in a random fashion, but show a prototypical progression (Braak and Braak, 1991; Braak et al., 2003; Brettschneider et al., 2015; Clavaguera et al., 2013). Relatedly, multimodal neuroimaging studies in humans have shown that the spatial patterns of brain atrophy (Lehmann et al., 2013b; Seeley et al., 2009; Zhou et al., 2012), glucose hypometabolism (Lehmann et al., 2013b; Raj et al., 2015) and Aβ (Buckner et al., 2005; Jones et al., 2016) bear strong anatomical resemblance to pre-existing brain networks. Together, these studies support a "network model" of neurodegeneration.

Several mechanisms have been proposed to explain network-based spread of disease, including "shared vulnerability" (i.e. neural

Abbreviations: AD, Alzheimer's disease; Aβ, Amyloid-β; CBS, Corticobasal syndrome; DVR, Distribution volume ratio; EOAD, Early-onset Alzheimer's disease; fMRI, Functional magnetic resonance imaging; GOF, Goodness-of-fit; ICN, Intrinsic connectivity network; LBNL, Lawrence Berkeley National Laboratory; LOAD, Late-onset Alzheimer's disease; lPCC, Left posterior cingulate cortex; lSTG, Left superior temporal gyrus; lvPPA, Logopenic variant primary progressive aphasia; MRI, Magnetic resonance imaging; PCA, Posterior cortical atrophy; PET, Positron emission tomography; rMFG, Right middle frontal gyrus; rMOG, Right middle occipital gyrus; ROI, region-of-interest; SPM, Statistical parametric mapping; SUVR, Standardized uptake value ratio; UCSF, University of California San Francisco

* Corresponding author at: Department of Neurology, Alzheimer Center, VU University Medical Center, De Boelelaan 1118, 1081 HZ Amsterdam, Netherlands.
E-mail address: r.ossenkoppele@vumc.nl (R. Ossenkoppele).

https://doi.org/10.1016/j.nicl.2019.101848
Received 26 September 2018; Received in revised form 2 April 2019; Accepted 1 May 2019
Available online 02 May 2019

populations with similar genetic and/or molecular properties may be equally susceptible, (Jackson, 2014), "wear and tear" (i.e. brain regions with high metabolic demands are most vulnerable to protein deposition, (Bero et al., 2011; Buckner et al., 2009; Jagust and Mormino, 2011; Kang et al., 2009), and "trans-neuronal spread" (i.e. cell-to-cell transmissibility of misfolded protein aggregates, (Baker et al., 1993; Frost and Diamond, 2010; Prusiner, 1984). The latter hypothesis has received considerable attention recently (Brettschneider et al., 2015; Clavaguera et al., 2015; Walsh and Selkoe, 2016) and is supported by experiments in transgenic mouse models demonstrating trans-synaptic spread of tau, α-synuclein and other misfolded protein aggregates (Clavaguera et al., 2013; de Calignon et al., 2012; Kaufman et al., 2016; Peeraer et al., 2015; Sanders et al., 2014).

Recent advances in human neuroimaging allow direct testing of this network model in living people. The three key elements of AD pathophysiology can now be quantified in vivo using [^{18}F]flortaucipir (hyper-phosphorylated tau filaments), [^{11}C]PIB (fibrillar Aβ plaques) and [^{18}F]FDG-PET (glucose hypometabolism, a marker of neurodegeneration), while the functional architecture of the brain can be evaluated using task-free fMRI. Previous [^{11}C]PIB-PET studies have revealed that Aβ is distributed diffusely throughout multimodal association cortex, and there are minimal inter-individual differences in Aβ patterns across AD patients, even in samples characterized by clinical and anatomical heterogeneity (Lehmann et al., 2013a; Ossenkoppele et al., 2012; Rabinovici et al., 2010). In contrast, studies with [^{18}F]flortaucipir-PET suggest that tau pathology is highly region-specific, co-localizes with sites of neurodegeneration as measured by [^{18}F]FDG-PET or structural MRI (assessing gray matter atrophy), and has a variable distribution across distinct clinical presentations and stages of AD (Cho et al., 2016; Johnson et al., 2016; Lowe et al., 2018; Mattsson et al., 2018; Ossenkoppele et al., 2018; Ossenkoppele et al., 2016; Pontecorvo et al., 2017; Scholl et al., 2016; Whitwell et al., 2018). These observations suggest that tau and Aβ are related but separated in space and time (Jack Jr. et al., 2018), which may have implications for understanding their spreading mechanisms. Neuropathological, neuroimaging and animal studies suggest differential regional susceptibility for early aggregation and mechanisms of spread for Aβ and tau (Buckner et al., 2009; Thal et al., 2015; Walsh and Selkoe, 2016). Secretion and aggregation of extra-cellular Aβ is associated with increased synaptic activity, and the widespread, multi-focal early distribution of Aβ plaques throughout the association cortex matches that of cortical "hubs" (i.e. highly connected brain regions). In contrast, intra-neuronal tau pathology may originate in a susceptible "epicenter" and spread trans-synaptically, following spatial patterns of pre-existing brain networks. Previous studies have provided preliminary in vivo evidence that [^{18}F]flortaucipir-PET uptake patterns show spatial overlap with functional networks (Cope et al., 2018; Hansson et al., 2017; Hoenig et al., 2018; Jones et al., 2017), using different approaches including independent component analysis, seed-based fMRI, goodness-of-fit with functional networks or graph theory approaches.

In this study, we used a seed-based approach to compare patterns of tau ([^{18}F]flortaucipir PET) and Aβ ([^{11}C]PIB) deposition and neurodegeneration (([^{18}F]FDG) in patients with AD to functional connectivity patterns identified with task-free fMRI in 1000 young adults. Building on previous studies, we sought to assess the relatedness of all three key elements of AD pathophysiology to the network structure of the brain in a relatively large cohort of patients enriched for clinical and neuroanatomical heterogeneity. We hypothesized that if protein deposition and subsequent neurodegeneration originate in distinct epicenters and then spread through functional networks, the covariance pattern of PET retention related to each seed should closely match the functional connectivity map from the same seed (Seeley et al., 2009). We hypothesized that tau pathology would show the best fit with functional connectivity maps, followed by hypometabolism (which may resemble the pattern of tau accumulation, though with lesser spatial extent due to a temporal delay between tau spread and neurodegeneration). Given the hypothesized differential origin and spreading mechanisms of Aβ pathology, we did not expect a specific match between the distribution of Aβ pathology and functional connectivity networks.

2. Materials and methods

2.1. Participants

A total of 63 patients were consecutively recruited from the University of California San Francisco (UCSF) Alzheimer's Disease Research Center between June 2014 and March 2018. All patients had 3 T MRI, [^{18}F]FDG PET, dynamic [^{11}C]PIB PET and [^{18}F]Flortaucipir PET available. Exclusion criteria were: 1) meeting core clinical criteria for another type of dementia, 2) clinically significant cerebrovascular disease, 3) major systemic disease, or 4) recent history of substance abuse. All patients underwent a medical history and physical examination, a structured caregiver interview, brain MRI and neuropsychological testing. All met clinical criteria for probable AD dementia (McKhann et al., 2011) (n = 54) or mild cognitive impairment due to AD (Albert et al., 2011) (n = 9) with supporting evidence of cerebral amyloidosis by a positive Aβ PET scan as determined by visual read (Ossenkoppele et al., 2016). Fifteen patients additionally met diagnostic criteria for posterior cortical atrophy (PCA, (Crutch et al., 2017)) and eight for logopenic-variant primary progressive aphasia (lvPPA, (Gorno-Tempini et al., 2011)). The remaining AD patients were classified as early-onset (EOAD, < 65 years at time of diagnosis, n = 23) or late-onset AD (LOAD, ≥65 years, n = 17). Note that all analyses were performed across the entire group of patients. We included a diverse population of AD patients in order to enrich the sample for heterogeneity in the expected patterns of tau distribution and neurodegeneration (Ossenkoppele et al., 2016; Pontecorvo et al., 2017; Whitwell et al., 2018). Informed consent was obtained from all patients or their assigned surrogate decision-makers, and UCSF and the Lawrence Berkeley National Laboratory (LBNL) institutional review boards for human research approved the study.

2.2. Structural MRI

All patients underwent MRI on a 3-Tesla Siemens Tim Trio scanner (Siemens, Erlangen, Germany). Sequences included T1-weighted magnetization prepared rapid gradient echo (MP-RAGE), which were processed using FreeSurfer 5.1 (Fischl et al., 2002) to define native-space reference regions and cortical regions-of-interest (ROIs).

2.3. PET

PET scans were performed at LBNL on a Siemens Biograph 6 Truepoint PET/CT scanner in 3D acquisition mode. A low-dose CT/transmission scan was performed for attenuation correction prior to all scans. [^{11}C]PIB and [^{18}F]Flortaucipir were synthesized and radiolabelled at LBNL's Biomedical Isotope Facility, whereas [^{18}F]FDG was provided by a commercial vendor (IBA Molecular). Ninety minutes of dynamic [^{11}C]PIB scan, 30 min of [^{18}F]FDG scan (t = 30–60 post-injection) and 20 min of [^{18}F]Flortaucipir scan (t = 80–100 min post-injection) were obtained for further processing (see section "Image analyses"). PET data were reconstructed using an ordered subset expectation maximization algorithm with weighted attenuation. Images were smoothed with a 4 mm Gaussian Kernel with scatter correction and evaluated prior to analysis for patient motion and adequacy of statistical counts. All PET scans were acquired within an average of 19.9 ± 8.9 days ([^{18}F]flortaucipir to [^{18}F]FDG: 29.8 ± 54.1, [^{18}F]flortaucipir to [^{11}C]PIB: 17.3 ± 52.4, [^{18}F]FDG to [^{11}C]PIB: 12.5 ± 25.0 days).

2.4. Image analyses

PET images were co-registered to the subjects' MP-RAGE using Statistical Parametric Mapping (SPM) version 12 (Wellcome Trust Centre for Neuroimaging, Institute of Neurology at University College London). Dynamic 90-min [^{11}C]PIB data were analyzed using Logan graphical analysis with FreeSurfer-derived gray matter cerebellum as the reference region, yielding voxelwise distribution volume ratio (DVR, (Logan et al., 1996)) images. [^{18}F]FDG PET images were summed, and standardized uptake value ratios (SUVR) were calculated for the 30–60 min post-injection interval using mean activity in the pons (manually edited from FreeSurfer-derived brainstem) as the reference region (Minoshima et al., 1995). Consistent with our previous studies (Baker et al., 2016; Ossenkoppele et al., 2015c; Scholl et al., 2016), SUVR images at t = 80–100 min post-injection were created by normalizing summed activity from the realigned frames to mean activity in inferior cerebellar gray matter (La Joie et al., 2018), an area relatively spared of neurofibrillary tangle pathology even in advanced AD (Braak and Braak, 1991; Marquie et al., 2015). Parametric PET images were spatially normalized to Montreal Neurological Institute space, followed by smoothing using an 8 mm isotropic Gaussian kernel.

For each participant, the corresponding structural T1 image was segmented into gray matter, white matter and cerebrospinal fluid compartments, which were used to estimate total intracranial volume (TIV) in SPM12 (Malone et al., 2015). Each individual gray matter image was modulated and smoothed with a 10.26 × 10.26 × 10.75 mm Gaussian kernel to match final PET resolution. Smoothed and modulated gray matter maps as well as TIV were used for all the PET covariance analyses (see below). All individual smoothed and modulated gray matter maps were averaged and thresholded at > 0.2 to create an explicit mask for the PET covariance analysis. Basal ganglia and cerebellum were manually removed from the mask.

2.5. Task-free functional MRI

We used task-free fMRI data of 1000 young adults (mean age: 21 ± 3), obtained through the Brain Genomic Superstruct Project and publicly available on an online platform (Neurosynth, www.neurosynth.org). All data were collected on matched 3 T Tim Trio scanners (Siemens, Erlangen, Germany) using a gradient-echo echo-planar imaging (EPI) sequence sensitive to blood oxygenation level-dependent (BOLD) contrast. Specifics on the fMRI pre-processing can be found elsewhere (Buckner et al., 2011; Choi et al., 2012; Yeo et al., 2011). We decided to include young controls rather than older controls or patient data because i) the large Neurosynth dataset maximizes generalizability of connectivity patterns in terms of how the average brain is functionally organized, ii) connectivity patterns in older subjects are susceptible to age-related pathological changes, and iii) connectivity in our AD patients is heavily impacted by the disease and are therefore not representative of normal brain architecture or of the architecture of their brain during time of protein spread.

2.6. Experimental design and statistical analysis

2.6.1. Seed-based fMRI and PET covariance analyses

2.6.1.1. Step 1. Defining seed regions. Fig. 1 depicts a schematic overview of the methodology. Analogous to the approach used by (Seeley et al., 2009) to identify vulnerable networks in distinct neurodegenerative diseases, we utilized "syndrome-specific epicenters" (i.e. epicenters specifically affected in AD variants, e.g. the left superior temporal gyrus seed in lvPPA to identify the language network) and "common epicenters" (i.e. epicenters affected across multiple AD variants, e.g. the left posterior cingulate seed to identify the posterior default-mode network) in seed-based intrinsic connectivity analyses. The first step was to define seed regions that account for both common and clinical variant-specific involvement of AD neurodegeneration. Consistent with previous work from our group (Lehmann et al., 2013a; Lehmann et al., 2013b), we used the common and syndrome-specific epicenters identified in an independent study assessing atrophy in different AD variants (Migliaccio et al., 2009). In that study, voxelwise contrasts of gray matter volumes between AD variants (i.e. PCA, lvPPA, EOAD and all variants combined) and healthy controls were performed. Syndrome specific epicenters were defined as regions that showed maximal atrophy (i.e. voxel with highest T-value) when contrasting a specific AD variant versus the others (e.g. PCA vs lvPPA/EOAD). The common epicenter was defined as the region that showed maximal atrophy when contrasting the convergent atrophy map of all AD syndromes to healthy controls. Peak atrophy voxels were located in the right middle occipital gyrus (rMOG) for PCA (MNI [x y z]: 39 -88 10), left superior temporal gyrus (lSTG) for lvPPA (-56 -40 1), right middle frontal gyrus (rMFG) for EOAD (40 42 30) and left posterior cingulate cortex (lPCC) across AD variants (-2 -33 28) (Migliaccio et al., 2009). We have previously shown that these epicenters robustly identify networks involved in specific AD phenotypes as well as across syndromes (Lehmann et al., 2013a; Lehmann et al., 2013b). Apart from the posterior cingulate cortex, we added two other common disease epicenters. First, given its importance in early phases of AD pathogenesis, we included a seed in the right medial temporal lobe (MTL), more specifically in the anterior hippocampus/amygdala transition area (25 -8 -18), based on a previous meta-analysis evaluating atrophy, hypometabolism and hypoperfusion studies in different stages of AD (Schroeter et al., 2009). Second, we defined a left post-central gyrus (PCG) seed (-39 -29 54), which is part of the sensorimotor system (Raichle, 2011) that is typically affected only in the most advanced stages of AD. For PET covariance analyses, we created regions-of-interest (ROIs) by drawing 4 mm spheres around these voxels, and calculated the mean SUVR (for [^{18}F]flortaucipir and [^{18}F]FDG) or DVR (for [^{11}C]PIB) in gray matter voxels within each ROI for all 63 AD patients.

2.6.1.2. Step 2. Voxelwise covariance analyses. In the second step, we performed voxelwise regression models using the Biological Parametric Mapping (BPM, (Casanova et al., 2007)) toolbox in SPM5 (BPM is not supported in more recent SPM versions) across patients to test for associations between the mean PET values within a seed region and the PET values for every cortical voxel across the brain (Lehmann et al., 2013a; Mechelli et al., 2005; Seeley et al., 2009). The BPM approach was selected since it offers the possibility to include individual voxelwise gray matter maps as *imaging* covariate, thereby controlling for potential modulating effects of atrophy on PET covariance patterns. Additionally, sex and age were included in all models as *non-imaging* covariates. All the regression models were performed using a robust regression (bisquare) approach (Yang et al., 2011). This was done using separate models for each seed and PET tracer combination (i.e. 6 seeds × 3 PET tracers = 18 models in total). For each of the six seeds, this approach resulted in distinct T-maps of covariance for the three PET tracers. To assess fMRI-based functional connectivity in young adults, we utilized the Neurosynth platform, which performs seed-based, voxelwise correlation analysis given the MNI coordinates of a single voxel as input. For each of our six seeds, this approach resulted in voxelwise functional connectivity maps of Pearson correlation coefficients. It is important to note that the PET covariance analyses explored correlations between seed region and each voxel *across subjects* only, while the fMRI analyses explored these correlations first *across time* (i.e. fMRI time series within subject), and secondly *across subjects*.

PET covariance analyses were performed using a seed-based approach at the voxel-level. By definition, other than distant findings, this analysis also returns evidence for significant association between signal in the seed and signal in voxels that are either belonging or are spatially proximal to the seed itself, a pattern referred to as *autocorrelation*. To investigate to what extent the observed effects were beyond that of *autocorrelation*, we assessed the associations between the magnitude of

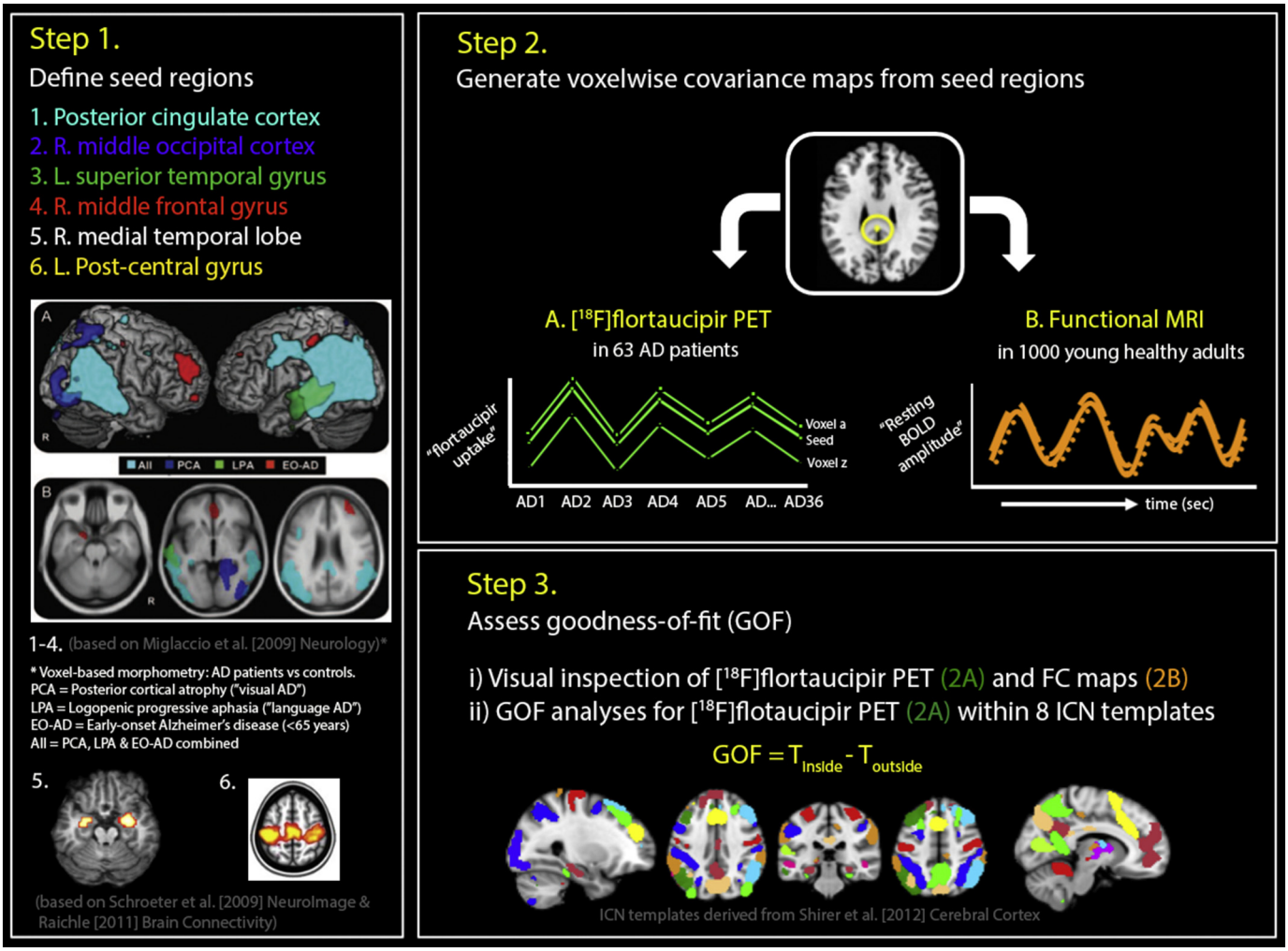

Fig. 1. Stepwise methods of the covariance approach.
First, six seed regions were selected based on the peak atrophy voxels in a previous study comparing AD variants against controls (step 1). The left panel figure shows brain templates with significant regions identified in the respective studies, and the actual coordinates of the seeds used in the current study are provided in the methods section. Next, these seed regions were used to generate voxelwise covariance maps for both [^{18}F]flortaucipir PET in 63 AD patients and task-free fMRI in 1000 young adults (step 2). Goodness-of-fit between the resulting [^{18}F]flortaucipir covariance and functional connectivity maps were then i) visually compared, and ii) more formally assessed in eight predefined intrinsic connectivity templates (step 3). Similar procedures were followed for [^{18}F]FDG and [^{11}C]PIB, instead of [^{18}F] flortaucipir, for secondary analyses.

observed PET covariance at each voxel and distance from the seed. We used R software (www.R-project.org, v3.4.4 for MAC OsX) and the *oro.nifti* and *fields* packages to create voxel-level maps of Euclidean distances from and for each seed. To move from voxel coordinates to real world MNI coordinates we used the affine transformation matrix, namely T = [−1.500,0,0,91.500,0,1.500,0,-127.500,0,0,1.500,-73.500,0,0,0,1.000]. The seed coordinates in MNI space were iteratively established by considering the locations of peak significance (e.g. the voxel with highest T-score for each model). This process led to the creation of $N = 6$ euclidean distance maps (one map for each seed) calculated over MNI space coordinates, and represented as millimeters (mm). We used a data driven approach to identify results that are likely due to autocorrelation. First, we identified the most restricted spatial pattern across the different 18 PET covariance models. This identification was performed both visually and quantitatively, the latter identifying the statistical model with the lowest number of voxels correlated with the seed. The most sparse pattern was then considered as the prototypical "autocorrelation-only" result. Subsequently, within this pattern/model, we considered the maximum Euclidean distance in which a significant effect (at $p < .05$ family-wise error (FWE) corrected, minimum cluster extent k = 100) was found. This Euclidean distance was then used as cut-off to define auto- and allo-correlation for all 18 PET x seed covariance models.

2.6.1.3. Step 3. Assessment of goodness-of-fit. In the final step we assessed GOF of PET covariance in three different ways. First, we thresholded the PET covariance T-maps (at $p < .05$, FWE corrected) and functional connectivity maps (at the default Neurosynth setting, i.e. Pearson $r \geq 0.2$), and visually assessed the convergence of PET covariance in AD patients and the functional architecture of young adults (Fig. 2). Second, we performed GOF analyses between PET covariance maps in AD patients (i.e. continuous non-thresholded maps) and eight intrinsic connectivity network templates that were developed by the Stanford Functional Imaging in Neuropsychiatric Disorders Lab (Shirer et al., 2012), and can be downloaded from http://findlap.stanford.edu/functional_ROIs.html. Note that we selected these network templates a priori, have used them in our previous work (Lehmann et al., 2013a; Lehmann et al., 2013b; Ossenkoppele et al., 2015a), and that functional networks are reproducible across centers and using different imaging modalities (Greicius et al., 2009; Hampson et al., 2002; Smith et al., 2009). GOF is expressed as the difference between the mean T-score of all voxels that fall within the network

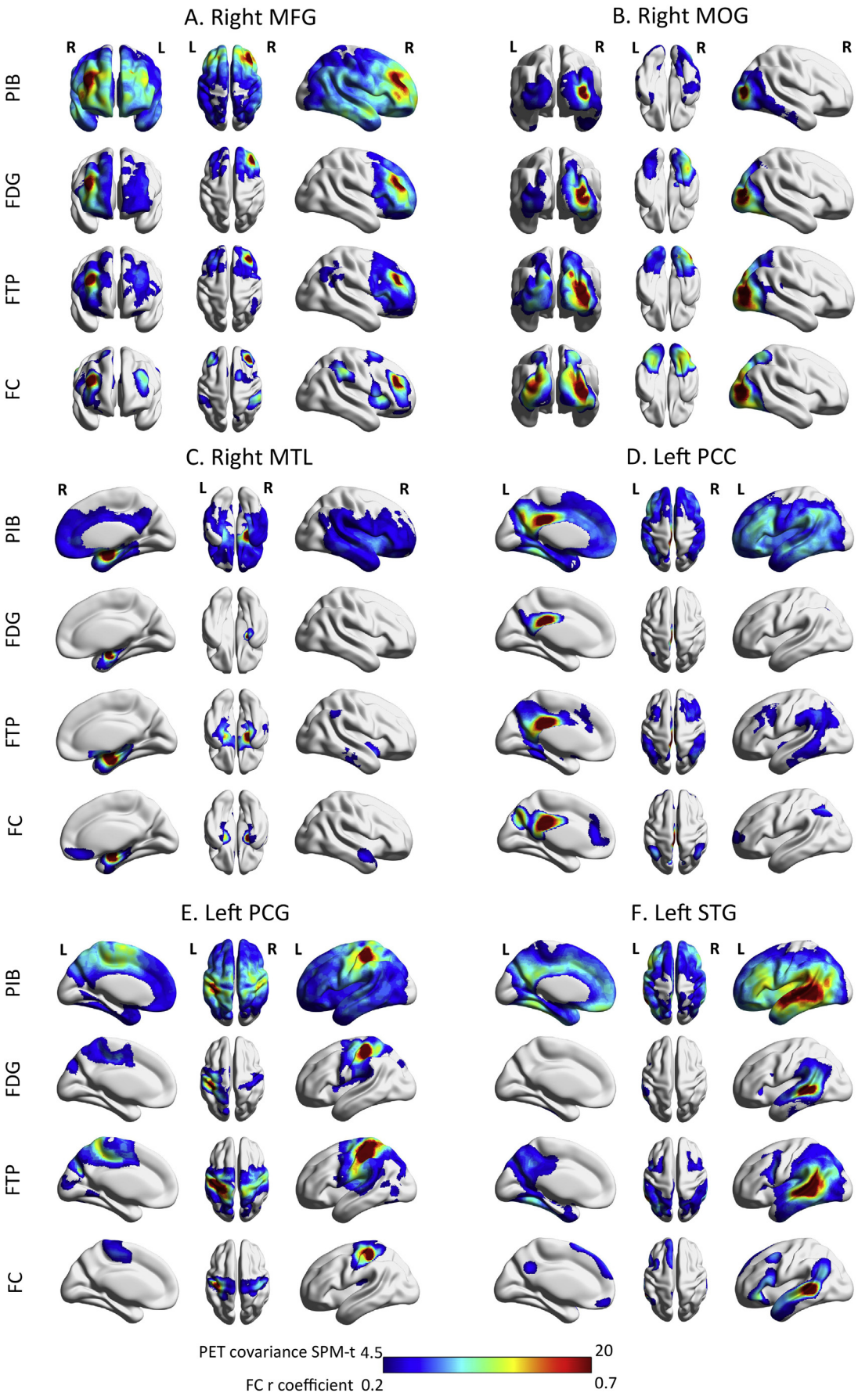

(caption on next page)

Fig. 2. [18F]flortaucipir/[18F]FDG/[11C]PIB covariance in AD vs functional connectivity in young adults.
[18F]Flortaucipir, [18F]FDG and [11C]PIB covariance (AD patients) and functional connectivity (young adults) maps are superimposed on a standard ICBM152 smoothed surface with BrainNet Viewer (Xia et al., 2013), thresholded at $p < .05$ family-wise error corrected ([18F]Flortaucipir, [18F]FDG and [11C]PIB) and at the default Neurosynth setting, i.e. Pearson $r \geq 0.2$ (fMRI). Color scales were set with maximum values at SPM-t = 20 and Pearson r = 0.7 for visualization purposes.
Legend: PIB = Pittsburgh Compound-B, FDG = Fluoro-deoxy glucose, FTP = [18F]Flortaucipir, FC = Functional Connectivity (maps), MFG = Middle Frontal Gyrus, MOG = Middle Occipital Gyrus, MTL = Medial Temporal Lobe, PCC = Posterior Cingulate Cortex, PoCG = Post-Central Gyrus, STG = Superior Temporal Gyrus.

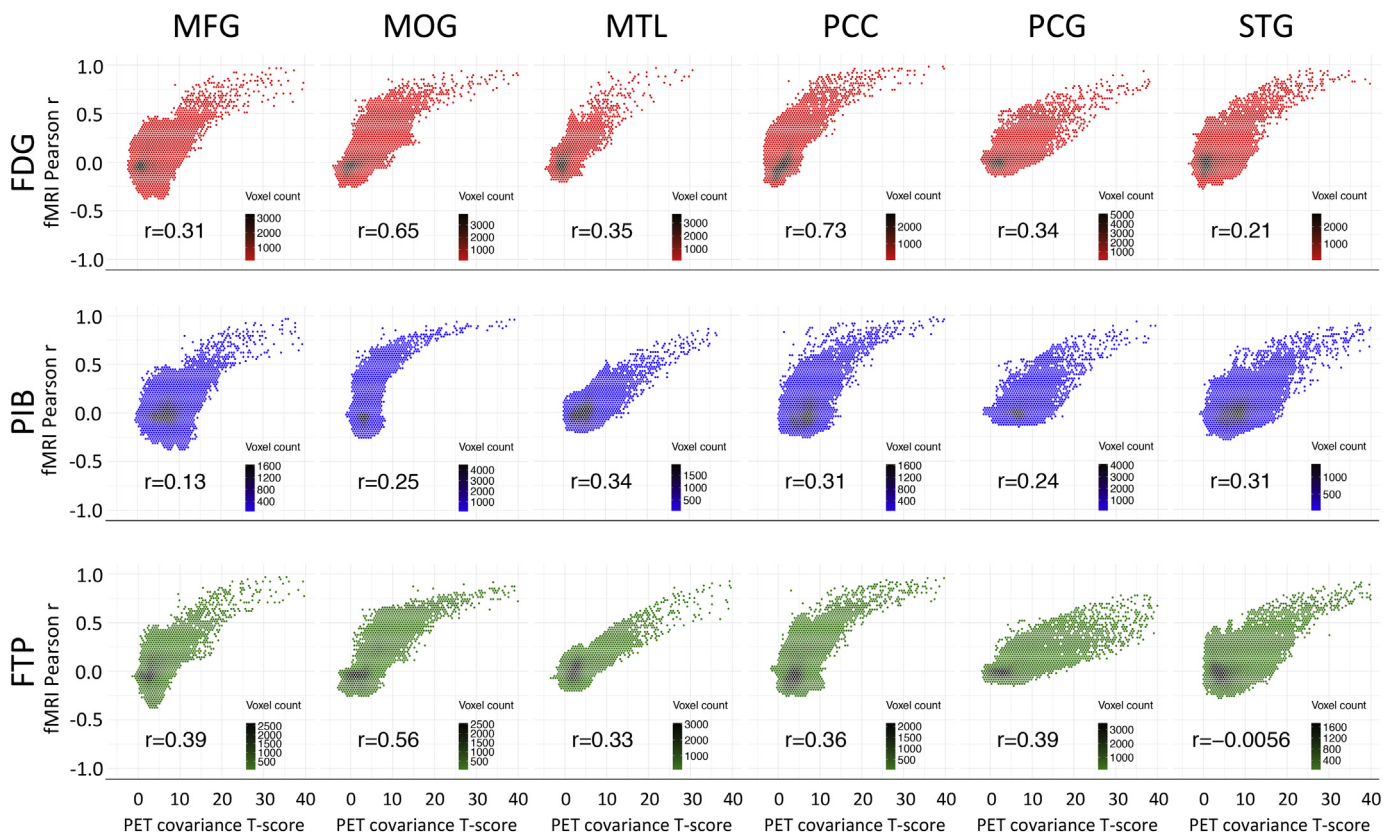

Fig. 3. Associations between PET covariance in AD patients and functional connectivity in young adults.
Hexed scatterplots showing the associations among PET covariance T-scores ([18F]FDG in red, [11C]PIB in blue, and [18F]Flortaucipir in green) in AD patients and fMRI Pearson r in young adults, considering all voxels within cortical gray matter. For each plot, the Spearman correlation coefficient between PET covariance and fMRI is provided. The shape and density of the hexagonal heatmaps indicate the strength of the relationship between the two modalities. For example, [18F]Flortaucipir and [18F]FDG covariance patterns in MOG show strong relationships with functional connectivity of the middle occipital cortex, whereas [11C]PIB shows a weaker association. The plots were generated with R software (r-project.org) and the *ggplot2* package.
Legend: PIB = Pittsburgh Compound-B, FDG = Fluoro-deoxy glucose, FTP = [18F]Flortaucipir, FC = Functional Connectivity (maps), MFG = Middle Frontal Gyrus, MOG = Middle Occipital Gyrus, MTL = Medial Temporal Lobe, PCC = Posterior Cingulate Cortex, PCG = Post-Central Gyrus, STG = Superior Temporal Gyrus.

template (T_{inside}) and the mean T-score of gray matter voxels outside the network template ($T_{outside}$), thus T_{inside} - $T_{outside}$. GOF values for all three PET tracers are presented in Table 2. Finally, we performed a post-hoc analysis to examine Spearman correlations between functional connectivity (Pearson r values) and PET covariance (T-values) maps (Fig. 3).

2.6.2. Sensitivity analyses

To examine the robustness of the findings we performed several sensitivity analyses for tau PET covariance patterns. First, we performed the same analyses but now without adjustment for age (thus only sex and GM volumes are included a covariates). Second, to exclude the possibility that results are completely driven by the patient population from which the seed regions were defined in an independent study (Migliaccio et al., 2009), we repeated the analyses for these seeds but excluded the respective patient group (e.g. PCA for the rMOG seed or lvPPA for the lSTG seed). Third, we aimed to provide additional support for the notion that tau pathology spreads trans-synaptically and not solely through proximity. We therefore selected four seeds from a previous study (Margulies et al., 2009) that were placed in the precuneus and yielded distinct (i.e. cognitive, visual, sensorimotor and limbic) functional networks in both humans and monkeys. Coordinates for the seeds are: cognitive (MNI [x y z]: -2 -58 37), visual (-1 -78 43), sensorimotor (-2 -47 58) and limbic (-2 -36 35). Similar to the original approach, we yielded for each seed both intrinsic functional connectivity maps in young adults and tau PET covariance patterns in patients with AD.

3. Results

3.1. Participants

Patients were relatively young (mean age at PET: 63 ± 8 years) and presented with a wide variety of clinical symptoms, including memory-predominant, visual (i.e. PCA, (Crutch et al., 2017)), language (i.e. lvPPA, (Gorno-Tempini et al., 2011)) and behavioral/dysexecutive (Ossenkoppele et al., 2015b) variants of AD. The 1000 healthy young adults for whom we utilized task-free functional MRI data had a mean age of 21 ± 3. Other participant characteristics are provided in Table 1.

Table 1
Demographic and clinical characteristics.

	AD patients	Controls
N	63 (n = 54 CE dementia, n = 9 MCI due to AD)	1000
Modality	[^{18}F]flortaucipir, [^{11}C]PIB & [^{18}F]FDG PET	Task-free functional MRI
Age (mean ± sd)	63.4 ± 8	21 ± 3 (range: 18–35)
Sex (m/f)	30/33	427/563
Education (mean ± sd)	16.9 ± 3.0	
CDR-Sum of boxes (mean ± sd)	4.2 ± 2.0	
MMSE (mean ± sd)	21.7 ± 5.4	
[^{11}C]PIB status	All positive	
Variant	Early-onset AD (n = 23) Late-onset AD (*n* = 17) Posterior cortical atrophy (*n* = 15) Logopenic variant PPA (*n* = 8)	

Abbreviations: AD = Alzheimer's disease; PIB = Pittsburgh compound B; CDR = Clinical dementia rating scale; FDG = Fluoro-deoxy glucose; MCI = Mild cognitive impairment; MRI = Magnetic resonance imaging; MMSE = Mini-mental state examination PET = Positron emission tomography; PPA = Primary progressive aphasia.

3.2. Overlap between PET covariance patterns and functional connectivity maps

To assess whether the distribution of tau pathology in AD patients follows the functional organization of the healthy brain, we selected six a priori defined disease epicenters as seed regions for PET and fMRI analyses related to AD (Fig. 1, step 1). The resulting covariance maps for [^{18}F]flortaucipir in AD and functional connectivity in healthy controls are displayed in Fig. 2. The results from this analysis showed a striking resemblance between the [^{18}F]flortaucipir covariance patterns across AD patients and the functional connectivity maps of young adults. The rMOG seed yielded [^{18}F]flortaucipir covariance and functional connectivity patterns that were mainly restricted to primary and association visual cortex, slightly extending into occipito-temporal areas (Fig. 2B). Maps derived from the lSTG seed showed predominant involvement of temporoparietal regions involved in language processes (left > right, Fig. 2F). The rMFG seed provided the strongest indication that tau pathology may spread in a network fashion as [^{18}F]flortaucipir covariance and functional connectivity maps showed cross-over from right to left dorsolateral prefrontal cortex as well as extension into non-spatially contiguous posterior parietal cortex, thereby “skipping over” the sensorimotor area (Fig. 2A). The lPCC seed-based analyses (Fig. 2D) resulted in an [^{18}F]flortaucipir covariance pattern that included the posterior cingulate cortex and precuneus, key hubs in the posterior default mode network (DMN). The rMTL seed yielded PET covariance and functional connectivity patterns that showed limited spatial extent and were mainly restricted to medial temporal lobe structures, extending into lateral temporal and parietal regions (Fig. 2C). The lPCG seed resulted in maps closely resembling the sensorimotor network (Fig. 2E).

We next assessed whether spatial patterns of Aβ and glucose hypometabolism across patients with AD showed differential overlap with brain functional connectivity. We therefore repeated the voxelwise covariance analyses for [^{11}C]PIB and [^{18}F]FDG. [^{18}F]FDG covariance maps closely resembled the maps derived from [^{18}F]flortaucipir, similarly overlapping with functional connectivity patterns although in a more spatially restricted manner (Fig. 2). For [^{11}C]PIB, most covariance maps showed widespread neocortical involvement that included many regions outside of the seed-specific functional connectivity map (Fig. 2). An exception was the rMOG seed, which yielded a [^{11}C]PIB covariance pattern that was spatially confined to posterior brain regions (Fig. 2B).

3.3. PET covariance and intrinsic connectivity network templates: goodness-of-fit analyses

To identify which canonical functional networks best matched the PET covariance patterns across AD patients, we followed an approach used in previous studies (Lehmann et al., 2013a; Lehmann et al., 2013b; Ossenkoppele et al., 2015a) and conducted goodness-of-fit analyses between covariance maps from each tracer and eight predefined intrinsic connectivity network templates (Shirer et al., 2012). The results (Table 2) indicated that [^{18}F]flortaucipir covariance patterns for each seed correlated most strongly with the ICN template that was previously linked to the seed in functional connectivity experiments (Lehmann et al., 2013b): higher-visual network for rMOG (GOF: 9.15), language network for lSTG (GOF: 5.50), right executive-control network for rMFG (GOF: 3.49), posterior DMN (GOF: 4.38) for lPCC and sensorimotor network (GOF: 7.03) for lPCG. Furthermore, the covariance patterns were specific to these ICN templates as indicated by the large differences in GOF between the network with the best fit and the remaining seven ICNs (Table 2). No specific pre-selected functional network provided a good fit with the [^{18}F]flortaucipir MTL covariance map (GOF for all networks < 0.70, Table 2). [^{18}F]FDG covariance maps showed the best GOF with the same ICN templates as [^{18}F]flortaucipir, although the strength of the GOF was slightly higher for [^{18}F]flortaucipir for most seed regions. [^{11}C]PIB covariance maps showed the best GOF with the same ICN templates identified using [^{18}F]flortaucipir and [^{18}F]FDG, although the magnitude of the GOF was generally lower than was observed with [^{18}F]flortaucipir and [^{18}F]FDG (Table 2).

3.4. Comparing strength of relationship with functional connectivity across PET tracers

As a complementary measure to compare [^{18}F]flortaucipir, [^{11}C]PIB and [^{18}F]FDG covariance with functional connectivity maps derived from each seed, we calculated voxelwise Spearman correlations between the ranked PET covariance T-scores and Pearson *r* values from the functional connectivity maps (Fig. 3, Table 3). For most seeds, [^{18}F]flortaucipir (range of Spearman coefficients: -0.01-0.56) and [^{18}F]FDG range of Spearman coefficients: 0.21–0.73) alternately showed highest correlations with functional connectivity maps in young adults (Fig. 3, Table 3), followed by [^{11}C]PIB (range of Spearman coefficients: 0.13–0.34), with the exception of the lSTG (for which [^{11}C]PIB showed the strongest correlation) and the rMTL (which was equivalent for the three PET tracers).

Table 2
Goodness-of-fit between [^{18}F]FDG, [^{11}C]PIB, and [^{18}F]flortaucipir covariance maps and intrinsic connectivity networks.

	Higher visual	Language	R. Executive-control	Posterior DMN	Sensorimotor	Ventral DMN	L. Executive-control	Salience
[^{18}F]flortaucipir								
R. middle occipital gyrus	**9.15**	−0.11	−1.38	0.47	0.49	1.03	1.04	−0.07
L. superior temporal gyrus	−0.38	**5.50**	−0.57	1.56	−1.80	0.88	0.74	1.68
R. middle frontal gyrus	−2.78	0.61	**3.49**	0.30	−0.92	0.29	1.10	0.44
L. Posterior cingulate cortex	−1.87	0.90	1.91	**4.38**	−2.00	1.87	0.80	1.31
L. Post central gyrus	−0.26	−0.22	−1.54	−0.45	**7.03**	0.30	−1.01	2.82
L. Medial temporal lobe	−0.47	−0.14	−0.10	0.46	−1.10	−0.02	−0.43	0.68
[^{18}F]FDG								
R. middle occipital gyrus	**8.16**	−0.89	−1.15	−0.92	−0.54	0.56	−2.33	−0.49
L. superior temporal gyrus	−1.01	**4.10**	−1.11	1.00	−0.59	−0.20	2.23	1.85
R. middle frontal gyrus	−3.03	0.05	**5.05**	−0.16	−1.08	−0.28	1.74	0.41
L. Posterior cingulate cortex	−1.70	0.31	1.33	**3.38**	−1.05	0.18	1.93	−0.57
L. Post central gyrus	−0.10	−0.28	−1.99	−0.86	**4.43**	−0.17	−0.60	1.14
L. Medial temporal lobe	−0.64	−0.88	−0.08	−0.40	−1.50	−0.81	−0.65	−0.85
[^{11}C]PIB								
R. middle occipital gyrus	**3.59**	0.47	−0.30	−0.06	−1.42	−0.08	0.14	−0.31
L. superior temporal gyrus	−2.54	**3.62**	−0.91	0.90	−2.56	−0.77	0.71	0.91
R. middle frontal gyrus	−2.29	0.82	**3.00**	−0.09	−1.71	−0.28	0.59	0.52
L. Posterior cingulate cortex	−2.43	1.61	−0.17	**3.18**	−2.22	0.00	0.77	0.85
L. Post central gyrus	−2.94	−0.09	0.15	−0.14	**3.81**	0.01	0.64	1.39
L. Medial temporal lobe	−2.08	0.87	−0.51	−0.14	−0.51	−1.01	−0.51	0.51

Table shows for each of the six seeds the goodness-of-fit between the [^{18}F]FDG, [^{11}C]PIB and [^{18}F]AV1451 covariance map and eight predefined intrinsic connectivity networks. Goodness-of-fit values represent the mean T-value of PET covariance within a network minus the mean T-value in gray matter voxels outside of the network. The numbers in bold represent for each network template the highest goodness-of-fit with a seed region.
Abbreviations: DMN = Default mode network; GOF = Goodness-of-fit; ICN = Intrinsic connectivity network; L = Left; R = Right.

Table 3
Spearman correlation coefficients between PET tracers and functional connectivity maps.

Seed	fMRI Pearson r versus:	Spearman's rho	Lower 95% CI	Upper 95% CI
MFG	[^{18}F]FDG	0.3076	0.3026	0.3125
MFG	[^{11}C]PIB	0.1342	0.1288	0.1395
MFG	[^{18}F]flortaucipir	0.3864	0.3820	0.3907
MOG	[^{18}F]FDG	0.6508	0.647	0.6544
MOG	[^{11}C]PIB	0.2514	0.2461	0.2569
MOG	[^{18}F]flortaucipir	0.5647	0.5606	0.5692
MTL	[^{18}F]FDG	0.3472	0.3423	0.3521
MTL	[^{11}C]PIB	0.3446	0.3397	0.3493
MTL	[^{18}F]flortaucipir	0.3336	0.3285	0.3383
PCC	[^{18}F]FDG	0.7257	0.7231	0.7283
PCC	[^{11}C]PIB	0.3072	0.3025	0.3122
PCC	[^{18}F]flortaucipir	0.3622	0.3576	0.3669
PCG	[^{18}F]FDG	0.3387	0.3338	0.3434
PCG	[^{11}C]PIB	0.2404	0.2352	0.2456
PCG	[^{18}F]flortaucipir	0.3894	0.3843	0.3944
STG	[^{18}F]FDG	0.2099	0.2046	0.2150
STG	[^{11}C]PIB	0.3131	0.3083	0.3179
STG	[^{18}F]flortaucipir	−0.0055	−0.0114	−0.0004

Table shows the Spearman correlation coefficients and 95% confidence intervals among PET covariance T-scores in AD patients and fMRI Pearson r in young adults, considering all voxels within cortical gray matter. The only non-significant difference between PET tracers within a seed is FDG vs PIB in the MTL (showing overlapping confidence intervals).
Abbreviations: CI = Confidence interval; MFG = Middle Frontal gyrus; MOG = Middle Occipital gyrus; MTL = Medial Temporal Lobe; PCC = Posterior Cingulate Cortex; PCG = Post central gyrus; STG = Superior Temporal gyrus.

3.5. Evaluating auto-correlation vs allo-correlation contributions in PET covariance

We aimed to determine the extent to which the observed effects were present beyond the effects of autocorrelation. The PET covariance model showing the least extended pattern was the [^{18}F]FDG-PET metabolic connectivity seeding in the right MTL (Fig. 2C). The peak T-score in the significant cluster at maximum distance from the seed was $T = 5.25$ (MNI coordinates 36–32 -15), located 26.37 mm from the seed. We then estimated the percentages of voxels that were significant (at $p < .05$ FWE-corrected) in the whole covariance maps and were closer or more distant than 26.37 mm from each respective seed. Both [^{11}C]PIB and [^{18}F]flortaucipir covariance maps showed more than half of the significant voxels to be allo-correlated for any of the seeds (Fig. 4 and Table 4), being systematically more diffuse than [^{18}F]FDG, except for the right MOG seed in which [^{11}C]PIB covariance showed the lowest percentage of allo-correlated voxels (~69%) as compared to [^{18}F]FDG (~73%) and to [^{18}F]flortaucipir (~84%). Except for the right MOG seed, all [^{11}C]PIB covariance maps showed the highest percentages of significant allo-correlated voxels (e.g. diffuse correlation voxel-wise), ranging from ~91% seeding from MTL to ~96% seeding from MFG (Fig. 4 and Table 4). [^{18}F]flortaucipir showed > 80% percentages of allo-correlated voxels except for the model seeding in the right MTL, where the percentage dropped to ~55%.

3.6. Sensitivity analyses

First, assessing tau PET covariance patterns without adjusting for age yielded similar results to the primary analyses in which age was included as a covariate, though in general the pattern was spatially more extended (Supplemental Fig. 1). Second, we found highly comparable results when excluding the patient population from which the seed regions were defined (e.g. PCA for the rMOG seed or lvPPA for the lSTG seed, Supplemental Fig. 2). Third, in addition to the six original seeds, we selected four seeds localized in the precuneus that previously yielded distinct functional networks in human and monkey brains (Margulies et al., 2009). We largely replicated the differential intrinsic functional connectivity networks (except for the sensorimotor network, see Fig. 3 in (Margulies et al., 2009) for comparison) and additionally found that the tau PET covariance patterns spatially overlapped with the cognitive, visual, sensorimotor and limbic networks (Supplemental Fig. 3).

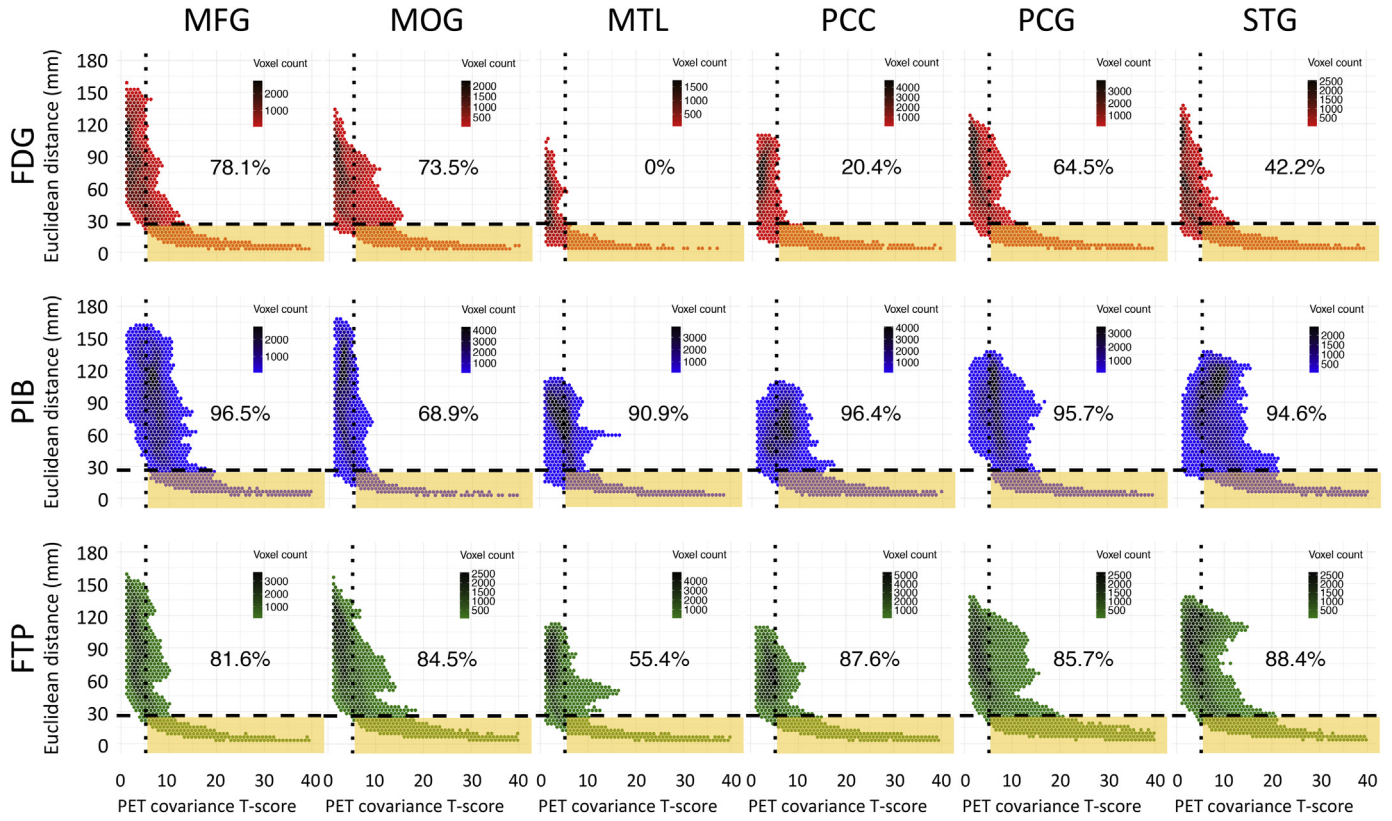

Fig. 4. Accounting for the effects of auto-correlation: Associations between PET covariance SPM-t scores and distance metrics.
Hexed scatterplots showing the associations among PET covariance T-scores ([^{18}F]FDG in red, [^{11}C]PIB in blue, and [^{18}F]Flortaucipir in green) in AD patients and Euclidean distance (millimeters) from the respective seed (see Materials and Methods for detailed information), considering all voxels within the cortical gray matter. For each model the percentage of *allo-correlated* voxels (i.e., *distant* voxels showing significant covariance with the seed) out of all significant voxels is shown (see also Table 4). Vertical dotted lines show the critical T-scores for the $P_{FWE} < 0.05$ SPM analysis for each model, while the horizontal dashed lines show the critical distance to define *auto-* vs. *allo*-correlation (i.e. 26.37 mm, see text for details on its derivation). For example, [^{18}F]FDG covariance in the MTL shows null *allo-correlation* (0%), whereas [^{11}C]PIB covariance in the MFG shows almost complete *allo*-correlation (96.5%). The orange shaded area highlights the *auto*-correlation quadrant (significant voxels close to the seed). The plots were generated with R software (r-project.org) and the *ggplot2* package.
Legend: PIB = Pittsburgh Compound-B, FDG = Fluoro-deoxy glucose, FTP = [^{18}F]Flortaucipir, FC = Functional Connectivity (maps), MFG = Middle Frontal Gyrus, MOG = Middle Occipital Gyrus, MTL = Medial Temporal Lobe, PCC = Posterior Cingulate Cortex, PCG = Post-Central Gyrus, STG = Superior Temporal Gyrus.

4. Discussion

According to the network model of neurodegeneration, the spread of pathogenic proteins occurs selectively along connected brain regions. We tested in vivo whether the distribution of filamentous tau (measured with [^{18}F]flortaucipir-PET), fibrillar amyloid-β ([^{11}C]PIB-PET) and glucose hypometabolism ([^{18}F]FDG-PET) in 63 patients with AD follows the intrinsic functional organization of the healthy brain. We selected six predefined disease epicenters for whole-brain voxelwise analyses to compare correlated patterns of [^{18}F]flortaucipir uptake across AD patients against fMRI intrinsic connectivity patterns in healthy young adults. We found a striking convergence between [^{18}F]flortaucipir covariance patterns and intrinsic connectivity maps, which corresponded with expected functional networks. [^{18}F]FDG covariance maps, which reflect neurodegenerative processes, showed similar but more spatially restricted patterns compared to [^{18}F]flortaucipir. Covariance maps of ([^{11}C]PIB (Aβ) were more diffuse, and although they showed the best GOF with the same ICN templates identified using [^{18}F]flortaucipir and [^{18}F]FDG, the strength and specificity of the GOF was generally lower than for [^{18}F]flortaucipir and [^{18}F]FDG. These

Table 4
Auto-correlation vs allo-correlation in the PET covariance models.

	R. MFG	R. MOG	R. MTL	L. PCC	L. PCG	L. STG
[^{18}F]FDG	32,237/41287 (78.1%)	22,813/31020 (73.5%)	0/2123 (0%)	898/4398 (20.4%)	17,304/26808 (64.5%)	7481/17744 (42.2%)
[^{11}C]PIB	254,524/263645 (96.5%)	15,134/21961 (68.9%)	129,303/142258 (90.9%)	228,731/237368 (96.4%)	250,727/261871 (95.7%)	257,601/272272 (94.6%)
[^{18}F]flortaucipir	39,459/48340 (81.6%)	48,877/57852 (84.5%)	9767/17638 (55.4%)	64,209/73282 (87.6%)	64,831/75613 (85.7%)	113,530/128361 (88.4%)

Table shows the ratio of *allo-correlated* voxels out of all the significant voxels for each PET modality by seed combination, plus the respective percentage. Auto-correlation distance threshold was defined as the maximum distance with a significant effect in the [^{18}F]FDG right MTL metabolic connectivity model, here thus showing 0% of allo-correlated voxels (see Material and Methods for details).
Abbreviations: MFG = Middle Frontal gyrus; MOG = Middle Occipital gyrus; MTL = Medial Temporal Lobe; PCC = Posterior Cingulate Cortex; PCG = Post central gyrus; STG = Superior Temporal gyrus.

findings suggest that the spatial patterns of tau pathology and neurodegeneration that are observed in AD follow the functional organization of the healthy brain, supporting the notion that tau pathology spreads through circumscribed brain networks and drives neurodegeneration. Conversely, Aβ patterns show a weaker and less specific relationship with brain connectivity and network architecture at the symptomatic stage of AD.

4.1. Tau covariance maps in AD match intrinsic connectivity networks in young adults

Filamentous tau assembled into neurofibrillary tangles is often considered the driving force behind neurodegeneration and cognitive decline in AD (Jack Jr. and Holtzman, 2013; Nelson et al., 2012; Spires-Jones and Hyman, 2014). For development of therapeutic agents, it is therefore important to understand the spreading mechanisms of tau pathology. The present findings are consistent with the "trans-synaptic spread" hypothesis, proposing that aggregates of misfolded tau move across synaptic connections and spread throughout the brain based on network architecture. This hypothesis is based on experiments showing cell-to-cell transmission of prion proteins and physical transfer of tau into downstream neurons after initial expression in the entorhinal cortex in AD transgenic mouse models (de Calignon et al., 2012; Kaufman et al., 2018; Liu et al., 2012). The striking resemblance between tau covariance in AD patients and functional connectivity maps in young adults, the clearly distinctive maps resulting from each seed, and the fact that the covariance patterns involve both hemispheres and leave proximate – yet less functionally connected – regions relatively unaffected (e.g. Fig. 2A and D) make our findings compatible with the mechanism of trans-synaptic spread. However, we only provide indirect evidence for this hypothesis and alternative models such as "shared vulnerability" between connected brain regions cannot be excluded. It should also be noted that for some seeds the tau PET covariance patterns exceeded the intrinsic connectivity maps, which might not be in full concordance with the trans-synaptic spread hypothesis. Observed differences between tau PET covariance and brain architecture may be caused by some spread through proximity to regions that fall outside the anatomical borders of the functional network. Alternatively, there is likely to be large inter-individual variation in intrinsic functional connectivity (and tau spread), while we evaluated the aggregate results across the entire group. Overall, our results are largely in line with previous studies (Cope et al., 2018; Hansson et al., 2017; Hoenig et al., 2018; Jones et al., 2016) showing overlap between Tau-PET patterns and functional networks, but the sample size of the AD group was larger than in previous studies and we enriched the sample with early-onset patients and non-amnestic variants to increase the regional variability in tau PET patterns (Ossenkoppele et al., 2016).

Braak staging of neurofibrillary pathology denotes early involvement of (trans)enthorinal cortex, followed by spread into limbic and para-limbic regions and finally neocortex (Braak and Braak, 1991). This pattern, which is consistent with trans-synaptic spread of tau, has largely been replicated by in vivo tau PET studies, though with some deviations (Cho et al., 2016; Scholl et al., 2016; Schwarz et al., 2016; Vogel et al., 2019). Compared to post-mortem investigations, brain imaging enables a more comprehensive comparison of spatial patterns of tau pathology (and other aspects of disease) to the network architecture of the brain, given the ability to sample the entire brain with different imaging modalities representing molecular pathology, brain structure and function. Early spread of tau within MTL circuits may not be clearly discernable with PET given the limited spatial resolution of the technique. The spread of tau from the MTL to more highly interconnected cortical hubs at later Braak stages (e.g. from anterior MTL regions to prefrontal cortex and from posterior MTL regions to medial parietal areas) may then further facilitate spreading of tau pathology into additional cortical networks, resulting in the patterns observed in the current study.

4.2. Glucose hypometabolism resembles tau patterns but is more spatially restricted

[^{18}F]FDG covariance patterns were similar to those observed for [^{18}F]flortaucipir, although more spatially restricted and with slightly lower goodness-of-fit. This is consistent with our previous study showing that nearly all hypometabolic regions contain high levels of tau pathology, while not all regions with high tau are hypometabolic (Ossenkoppele et al., 2016). Though our study is cross-sectional, these findings suggest that tau pathology is spreading through a functional network with neurodegeneration lagging behind, presumably following the topography of tau with a temporal delay. Longitudinal data are needed to confirm these relationships.

4.3. Topography of Aβ covariance is more diffuse than that of tau and hypometabolism

Several studies have shown transneuronal spread of Aβ in transgenic mouse models, raising the possibility of network-based spread of amyloid pathology (Baker et al., 1993; Meyer-Luehmann et al., 2006; Rosen et al., 2012). We found that [^{11}C]PIB covariance patterns were more diffuse (Fig. 2) and – although high – generally showed lower goodness-of-fit with functional connectivity maps compared to [^{18}F]flortaucipir and [^{18}F]FDG (Table 2). There are several possible explanations for this. First, there is compelling evidence that extracellular Aβ preferentially deposits in highly connected brain regions ("hubs"), which are also characterized by high metabolic demands. For example, animal models have shown that increased neuronal activity is associated with greater Aβ secretion and aggregation (Bero et al., 2011; Kang et al., 2009), while human neuroimaging studies showed strong spatial correlations between [^{11}C]PIB retention and levels of aerobic glycolysis (Vlassenko et al., 2010) and overall degree of connectivity (or "hubness") (Buckner et al., 2009; Sepulcre et al., 2013). Furthermore, [^{11}C]PIB studies in preclinical AD suggest that early Aβ accumulation appears to emerge synchronously in multiple cortical hubs, such as posterior cingulate/precuneus and medial prefrontal cortex (Villeneuve et al., 2015). Therefore, it may be that a shared vulnerability determines the widespread and multi-focal onset of Aβ, in contrast with tau pathology, which originates in only a few regions. As such, Aβ aggregation may involve multiple brain networks even at the earliest stages, with subsequent spreading through these networks or in the extra-cellular space. Alternatively, both Aβ and tau pathologies could originate from specific epicenters and subsequently spread through functional networks. At the dementia stage, however, this process could be masked for Aβ spreading, which may have preceded the spread of tau by years and is diffusely deposited across large areas of the neocortex even in preclinical stages of AD (Villeneuve et al., 2015). Therefore, the lower specificity of Aβ covariance patterns compared to tau and FDG-PET in symptomatic AD patients may be a consequence of disease stage rather than mechanism of spread. In summary, our data could be consistent with early network-specific spread of Aβ, and both multi-focal and epicenter-based models of spread are equally supported by our results.

The one exception to the generally diffuse patterns of [^{11}C]PIB covariance was the map derived from the right middle occipital cortex seed, which yielded a covariance map spatially confined to posterior brain regions (Fig. 2B). Amyloid accumulation in occipital cortex may reflect more advanced disease (Villeneuve et al., 2015), thus more restricted covariance patterns may reflect later stage amyloid accumulation. Alternatively, occipital [^{11}C]PIB signal may primarily reflect cerebral amyloid angiopathy, which has a predilection for the occipital cortex (Johnson et al., 2007), binds [^{11}C]PIB (Ducharme et al., 2013) and is present in a majority of patients with AD (Jellinger, 2002). Thus, this restricted covariance pattern may reflect a distinct form of Aβ aggregation. An unexpected finding was that the correlation coefficients for the lSTG seed were higher for PIB PET compared to tau PET

covariance patterns (Fig. 3). It should be noted, however, that the correlation for the lSTG seed was decreased ($r = -0.01$) for tau PET covariance compared to the other seeds ($r = 0.33$–0.56) rather than elevated for PIB PET ($r = 0.31$ for lSTG versus $r = 0.13$–0.34 for the other seeds). Furthermore, goodness-of-fit with the language network was still higher for tau and FDG PET compared to PIB PET (Table 2).

4.4. Strengths and limitations

Strengths of our study include the availability of combined tau, Aβ and glucose hypometabolism PET measurements in a heterogeneous population of AD patients (allowing sampling from a wide variability of PET patterns) and the use of a priori defined seed regions and ICN templates (Lehmann et al., 2013a; Ossenkoppele et al., 2015a; Shirer et al., 2012). There are also several weaknesses. First, this is a cross-sectional study, and longitudinal studies are needed to determine the exact nature of tau pathological progression over time. Second, based on previous work from our group and others (Jones et al., 2016; Lehmann et al., 2013a; Lehmann et al., 2013b; Seeley et al., 2009), we used the functional architecture as a surrogate for the structural connectome. Direct comparisons between intrinsic connectivity (measured with resting-state fMRI) and structural connectivity (derived from DTI) yielded largely convergent results (Greicius et al., 2009), but their relationships are still debated and each imaging modality likely indicates partly distinct properties of large-scale brain networks (Reijmer et al., 2015; Wang et al., 2015). Future studies relating tau PET to structural connectivity – in addition to functional connectivity - are therefore warranted. Third, although epicenter defined seed-based analyses are commonly used to approximate regions of disease origin or early vulnerability, it should be acknowledged that the disease does not necessarily have to begin in the seed location. Fourth, one should be careful assuming homogeneity of functional connections and understand that functional connections will change as a consequence of the disease (Menkes-Caspi et al., 2015) or chronological aging (Damoiseaux et al., 2008). These changes were not taken into account in this study since we used functional connectivity maps from young healthy adults. Fifth, we compared topographic overlap between functional networks in healthy adults and PET covariance across AD patients, but the interpretation is limited as we could not determine the specificity of brain network architecture across multiple biological scales. Sixth, although we performed sensitivity analyses in subgroups, the inclusion of many EOAD cases may limit generalizability to a strictly LOAD population in which the tau PET patterns are generally more restricted than in EOAD patients (Scholl et al., 2017; Tetzloff et al., 2018). Seventh, we did not formally test differences between PET tracers because GOF analysis does not provide an error term and very minor differences in Spearman correlation coefficients reached statistical significance due to the large number of tests (i.e. tens of thousands of voxels in our brain mask, see Table 3). Finally, some tracer-specific properties should be considered. [^{11}C]PIB only binds fibrillar Aβ and not the more toxic oligomeric species, which may have attenuated the relationships between [^{11}C]PIB covariance and functional connectivity. [^{18}F]flortaucipir is a relatively new tracer, thus only few ante-mortem vs post-mortem comparisons have been reported (Lowe et al., 2016; Marquie et al., 2015; Sander et al., 2016) and its binding properties are not yet fully understood.

4.5. Future directions

Longitudinal multi-modality PET imaging in combination with functional MRI will help address fundamental questions about the mechanisms that drive the spread of core protein aggregates in AD. Key topics for future research include building more advanced computational models using graph theoretical metrics and predicting individual patterns of longitudinal Aβ, tau and neurodegeneration based on baseline individual patterns (Braga and Buckner, 2017; Bullmore and Sporns, 2009; Raj et al., 2015; Zhou et al., 2012). If tau pathology truly spreads trans-synaptically through poly-synaptic links, it could be hypothesized that intermediate nodes in a brain network would accumulate tau pathology prior to more distal nodes.

5. Conclusion

Our findings suggest that the spatial patterns of tau and glucose hypometabolism observed in AD resemble the functional organization of the healthy brain, supporting the notion that tau pathology spreads through circumscribed brain networks and drives neurodegeneration.

Supplementary data to this article can be found online at https://doi.org/10.1016/j.nicl.2019.101848.

Acknowledgements

We would like to thank Nagehan Ayakta, Averill Cantwell, Jamie Faria, Allison Fero Andreas Lazaris, Kristin Norton, and Vyoma Shah for their contributions in the acquisition and analysis of PET data. This research was funded by Marie Curie FP7 International Outgoing Fellowship [628812] (to R.O.); The donors of [Alzheimer's Disease Research], a program of BrightFocus Foundation (to R.O.); Tau Consortium (to G.D.R. and W.J.J); National Institute on Aging grants [R01-AG045611] (to G.D.R.), [R01-AG034570] (to W.J.J.), [P50-AG023501] (to G.D.R, H.J.R. and B.L.M; John Douglas French Alzheimer's Foundation (to G.D.R. and B.L.M.); State of California Department of Health Services Alzheimer's Disease Research Center of California grant [04-33516] (to B.L.M). Avid Radiopharmaceuticals enabled use of the [^{18}F]flortaucipir tracer, but did not provide direct funding and was not involved in data analysis or interpretation.

Conflict of interest

The authors declare no competing financial interests.

References

Albert, M.S., DeKosky, S.T., Dickson, D., Dubois, B., Feldman, H.H., Fox, N.C., Gamst, A., Holtzman, D.M., Jagust, W.J., Petersen, R.C., Snyder, P.J., Carrillo, M.C., Thies, B., Phelps, C.H., 2011. The diagnosis of mild cognitive impairment due to Alzheimer's disease: recommendations from the National Institute on Aging-Alzheimer's Association workgroups on diagnostic guidelines for Alzheimer's disease. Alzheimers Dement. 7, 270–279.

Baker, H.F., Ridley, R.M., Duchen, L.W., Crow, T.J., Bruton, C.J., 1993. Evidence for the experimental transmission of cerebral beta-amyloidosis to primates. Int. J. Exp. Pathol. 74, 441–454.

Baker, S.L., Lockhart, S.N., Price, J.C., He, M., Huesman, R.H., Schonhaut, D., Faria, J., Rabinovici, G., Jagust, W.J., 2016. Reference tissue-based kinetic evaluation of 18F-AV-1451 in aging and dementia. J. Nucl. Med. 58, 332–338.

Bero, A.W., Yan, P., Roh, J.H., Cirrito, J.R., Stewart, F.R., Raichle, M.E., Lee, J.M., Holtzman, D.M., 2011. Neuronal activity regulates the regional vulnerability to amyloid-beta deposition. Nat. Neurosci. 14, 750–756.

Braak, H., Braak, E., 1991. Neuropathological stageing of Alzheimer-related changes. Acta Neuropathol. 82, 239–259.

Braak, H., Del Tredici, K., Rub, U., de Vos, R.A., Jansen Steur, E.N., Braak, E., 2003. Staging of brain pathology related to sporadic Parkinson's disease. Neurobiol. Aging 24, 197–211.

Braga, R.M., Buckner, R.L., 2017. Parallel interdigitated distributed networks within the individual estimated by intrinsic functional connectivity. Neuron 95, 457–471 (e455).

Brettschneider, J., Del Tredici, K., Lee, V.M., Trojanowski, J.Q., 2015. Spreading of pathology in neurodegenerative diseases: a focus on human studies. Nat. Rev. Neurosci. 16, 109–120.

Buckner, R.L., Snyder, A.Z., Shannon, B.J., LaRossa, G., Sachs, R., Fotenos, A.F., Sheline, Y.I., Klunk, W.E., Mathis, C.A., Morris, J.C., Mintun, M.A., 2005. Molecular, structural, and functional characterization of Alzheimer's disease: evidence for a relationship between default activity, amyloid, and memory. J. Neurosci. 25, 7709–7717.

Buckner, R.L., Sepulcre, J., Talukdar, T., Krienen, F.M., Liu, H., Hedden, T., Andrews-Hanna, J.R., Sperling, R.A., Johnson, K.A., 2009. Cortical hubs revealed by intrinsic functional connectivity: mapping, assessment of stability, and relation to Alzheimer's disease. J. Neurosci. 29, 1860–1873.

Buckner, R.L., Krienen, F.M., Castellanos, A., Diaz, J.C., Yeo, B.T., 2011. The organization of the human cerebellum estimated by intrinsic functional connectivity. J. Neurophysiol. 106, 2322–2345.

Bullmore, E., Sporns, O., 2009. Complex brain networks: graph theoretical analysis of

structural and functional systems. Nat. Rev. Neurosci. 10, 186–198.
Casanova, R., Srikanth, R., Baer, A., Laurienti, P.J., Burdette, J.H., Hayasaka, S., Flowers, L., Wood, F., Maldjian, J.A., 2007. Biological parametric mapping: a statistical toolbox for multimodality brain image analysis. Neuroimage 34, 137–143.
Cho, H., Choi, J.Y., Hwang, M.S., Kim, Y.J., Lee, H.M., Lee, H.S., Lee, J.H., Ryu, Y.H., Lee, M.S., Lyoo, C.H., 2016. In vivo cortical spreading pattern of tau and amyloid in the Alzheimer disease spectrum. Ann. Neurol. 80, 247–258.
Choi, E.Y., Yeo, B.T., Buckner, R.L., 2012. The organization of the human striatum estimated by intrinsic functional connectivity. J. Neurophysiol. 108, 2242–2263.
Clavaguera, F., Akatsu, H., Fraser, G., Crowther, R.A., Frank, S., Hench, J., Probst, A., Winkler, D.T., Reichwald, J., Staufenbiel, M., Ghetti, B., Goedert, M., Tolnay, M., 2013. Brain homogenates from human tauopathies induce tau inclusions in mouse brain. Proc. Natl. Acad. Sci. U. S. A. 110, 9535–9540.
Clavaguera, F., Hench, J., Goedert, M., Tolnay, M., 2015. Invited review: prion-like transmission and spreading of tau pathology. Neuropathol. Appl. Neurobiol. 41, 47–58.
Cope, T.E., Rittman, T., Borchert, R.J., Jones, P.S., Vatansever, D., Allinson, K., Passamonti, L., Vazquez Rodriguez, P., Bevan-Jones, W.R., O'Brien, J.T., Rowe, J.B., 2018. Tau burden and the functional connectome in Alzheimer's disease and progressive supranuclear palsy. Brain 141, 550–567.
Crutch, S.J., Schott, J.M., Rabinovici, G.D., Murray, M., Snowden, J.S., van der Flier, W.M., Dickerson, B.C., Vandenberghe, R., Ahmed, S., Bak, T.H., Boeve, B.F., Butler, C., Cappa, S.F., Ceccaldi, M., de Souza, L.C., Dubois, B., Felician, O., Galasko, D., Graff-Radford, J., Graff-Radford, N.R., Hof, P.R., Krolak-Salmon, P., Lehmann, M., Magnin, E., Mendez, M.F., Nestor, P.J., Onyike, C.U., Pelak, V.S., Pijnenburg, Y., Primativo, S., Rossor, M.N., Ryan, N.S., Scheltens, P., Shakespeare, T.J., Suarez Gonzalez, A., Tang-Wai, D.F., Yong, K.X., Carrillo, M., Fox, N.C., Alzheimer's Association, I.A.A.s.D., Associated Syndromes Professional Interest, A, 2017. Consensus classification of posterior cortical atrophy. Alzheimers Dement. 13, 870–884.
Damoiseaux, J.S., Beckmann, C.F., Arigita, E.J., Barkhof, F., Scheltens, P., Stam, C.J., Smith, S.M., Rombouts, S.A., 2008. Reduced resting-state brain activity in the "default network" in normal aging. Cereb. Cortex 18, 1856–1864.
de Calignon, A., Polydoro, M., Suarez-Calvet, M., William, C., Adamowicz, D.H., Kopeikina, K.J., Pitstick, R., Sahara, N., Ashe, K.H., Carlson, G.A., Spires-Jones, T.L., Hyman, B.T., 2012. Propagation of tau pathology in a model of early Alzheimer's disease. Neuron 73, 685–697.
Ducharme, S., Guiot, M.C., Nikelski, J., Chertkow, H., 2013. Does a positive Pittsburgh compound B scan in a patient with dementia equal Alzheimer disease? JAMA Neurol 70, 912–914.
Fischl, B., Salat, D.H., Busa, E., Albert, M., Dieterich, M., Haselgrove, C., van der Kouwe, A., Killiany, R., Kennedy, D., Klaveness, S., Montillo, A., Makris, N., Rosen, B., Dale, A.M., 2002. Whole brain segmentation: automated labeling of neuroanatomical structures in the human brain. Neuron 33, 341–355.
Frost, B., Diamond, M.I., 2010. Prion-like mechanisms in neurodegenerative diseases. Nat. Rev. Neurosci. 11, 155–159.
Gorno-Tempini, M.L., Hillis, A.E., Weintraub, S., Kertesz, A., Mendez, M., Cappa, S.F., Ogar, J.M., Rohrer, J.D., Black, S., Boeve, B.F., Manes, F., Dronkers, N.F., Vandenberghe, R., Rascovsky, K., Patterson, K., Miller, B.L., Knopman, D.S., Hodges, J.R., Mesulam, M.M., Grossman, M., 2011. Classification of primary progressive aphasia and its variants. Neurology 76, 1006–1014.
Greicius, M.D., Supekar, K., Menon, V., Dougherty, R.F., 2009. Resting-state functional connectivity reflects structural connectivity in the default mode network. Cereb. Cortex 19, 72–78.
Hampson, M., Peterson, B.S., Skudlarski, P., Gatenby, J.C., Gore, J.C., 2002. Detection of functional connectivity using temporal correlations in MR images. Hum. Brain Mapp. 15, 247–262.
Hansson, O., Grothe, M.J., Strandberg, T.O., Ohlsson, T., Hagerstrom, D., Jogi, J., Smith, R., Scholl, M., 2017. Tau pathology distribution in Alzheimer's disease corresponds differentially to cognition-relevant functional brain networks. Front. Neurosci. 11, 167.
Hoenig, M.C., Bischof, G.N., Seemiller, J., Hammes, J., Kukolja, J., Onur, O.A., Jessen, F., Fliessbach, K., Neumaier, B., Fink, G.R., van Eimeren, T., Drzezga, A., 2018. Networks of tau distribution in Alzheimer's disease. Brain 141, 568–581.
Jack Jr., C.R., Holtzman, D.M., 2013. Biomarker modeling of Alzheimer's disease. Neuron 80, 1347–1358.
Jack Jr., C.R., Wiste, H.J., Schwarz, C.G., Lowe, V.J., Senjem, M.L., Vemuri, P., Weigand, S.D., Therneau, T.M., Knopman, D.S., Gunter, J.L., Jones, D.T., Graff-Radford, J., Kantarci, K., Roberts, R.O., Mielke, M.M., Machulda, M.M., Petersen, R.C., 2018. Longitudinal tau PET in ageing and Alzheimer's disease. Brain 141, 1517–1528.
Jackson, W.S., 2014. Selective vulnerability to neurodegenerative disease: the curious case of prion protein. Dis. Model. Mech. 7, 21–29.
Jagust, W.J., Mormino, E.C., 2011. Lifespan brain activity, beta-amyloid, and Alzheimer's disease. Trends Cogn. Sci. 15, 520–526.
Jellinger, K.A., 2002. Alzheimer disease and cerebrovascular pathology: an update. J. Neural Transm. (Vienna) 109, 813–836.
Johnson, K.A., Gregas, M., Becker, J.A., Kinnecom, C., Salat, D.H., Moran, E.K., Smith, E.E., Rosand, J., Rentz, D.M., Klunk, W.E., Mathis, C.A., Price, J.C., Dekosky, S.T., Fischman, A.J., Greenberg, S.M., 2007. Imaging of amyloid burden and distribution in cerebral amyloid angiopathy. Ann. Neurol. 62, 229–234.
Johnson, K.A., Schultz, A., Betensky, R.A., Becker, J.A., Sepulcre, J., Rentz, D., Mormino, E., Chhatwal, J., Amariglio, R., Papp, K., Marshall, G., Albers, M., Mauro, S., Pepin, L., Alverio, J., Judge, K., Philiossaint, M., Shoup, T., Yokell, D., Dickerson, B., Gomez-Isla, T., Hyman, B., Vasdev, N., Sperling, R., 2016. Tau positron emission tomographic imaging in aging and early Alzheimer disease. Ann. Neurol. 79, 110–119.
Jones, D.T., Knopman, D.S., Gunter, J.L., Graff-Radford, J., Vemuri, P., Boeve, B.F., Petersen, R.C., Weiner, M.W., Jack Jr., C.R., Alzheimer's Disease Neuroimaging, I, 2016. Cascading network failure across the Alzheimer's disease spectrum. Brain 139, 547–562.
Jones, D.T., Graff-Radford, J., Lowe, V.J., Wiste, H.J., Gunter, J.L., Senjem, M.L., Botha, H., Kantarci, K., Boeve, B.F., Knopman, D.S., Petersen, R.C., Jack Jr., C.R., 2017. Tau, amyloid, and cascading network failure across the Alzheimer's disease spectrum. Cortex 97, 143–159.
Kang, J.E., Lim, M.M., Bateman, R.J., Lee, J.J., Smyth, L.P., Cirrito, J.R., Fujiki, N., Nishino, S., Holtzman, D.M., 2009. Amyloid-beta dynamics are regulated by orexin and the sleep-wake cycle. Science 326, 1005–1007.
Kaufman, S.K., Sanders, D.W., Thomas, T.L., Ruchinskas, A.J., Vaquer-Alicea, J., Sharma, A.M., Miller, T.M., Diamond, M.I., 2016. Tau prion strains dictate patterns of cell pathology, progression rate, and regional vulnerability in vivo. Neuron 92, 796–812.
Kaufman, S.K., Del Tredici, K., Thomas, T.L., Braak, H., Diamond, M.I., 2018. Tau seeding activity begins in the transentorhinal/entorhinal regions and anticipates phospho-tau pathology in Alzheimer's disease and PART. Acta Neuropathol. 136, 57–67.
La Joie, R., Bejanin, A., Fagan, A.M., Ayakta, N., Baker, S.L., Bourakova, V., Boxer, A.L., Cha, J., Karydas, A., Jerome, G., Maass, A., Mensing, A., Miller, Z.A., O'Neil, J.P., Pham, J., Rosen, H.J., Tsai, R., Visani, A.V., Miller, B.L., Jagust, W.J., Rabinovici, G.D., 2018. Associations between [(18)F]AV1451 tau PET and CSF measures of tau pathology in a clinical sample. Neurology 90, e282–e290.
Lehmann, M., Ghosh, P.M., Madison, C., Laforce Jr., R., Corbetta-Rastelli, C., Weiner, M.W., Greicius, M.D., Seeley, W.W., Gorno-Tempini, M.L., Rosen, H.J., Miller, B.L., Jagust, W.J., Rabinovici, G.D., 2013a. Diverging patterns of amyloid deposition and hypometabolism in clinical variants of probable Alzheimer's disease. Brain 136, 844–858.
Lehmann, M., Madison, C.M., Ghosh, P.M., Seeley, W.W., Mormino, E., Greicius, M.D., Gorno-Tempini, M.L., Kramer, J.H., Miller, B.L., Jagust, W.J., Rabinovici, G.D., 2013b. Intrinsic connectivity networks in healthy subjects explain clinical variability in Alzheimer's disease. Proc. Natl. Acad. Sci. U. S. A. 110, 11606–11611.
Liu, L., Drouet, V., Wu, J.W., Witter, M.P., Small, S.A., Clelland, C., Duff, K., 2012. Trans-synaptic spread of tau pathology in vivo. PLoS One 7, e31302.
Logan, J., Fowler, J.S., Volkow, N.D., Wang, G.J., Ding, Y.S., Alexoff, D.L., 1996. Distribution volume ratios without blood sampling from graphical analysis of PET data. J. Cereb. Blood Flow Metab. 16, 834–840.
Lowe, V.J., Curran, G., Fang, P., Liesinger, A.M., Josephs, K.A., Parisi, J.E., Kantarci, K., Boeve, B.F., Pandey, M.K., Bruinsma, T., Knopman, D.S., Jones, D.T., Petrucelli, L., Cook, C.N., Graff-Radford, N.R., Dickson, D.W., Petersen, R.C., Jack Jr., C.R., Murray, M.E., 2016. An autoradiographic evaluation of AV-1451 tau PET in dementia. Acta Neuropathol Commun 4, 58.
Lowe, V.J., Wiste, H.J., Senjem, M.L., Weigand, S.D., Therneau, T.M., Boeve, B.F., Josephs, K.A., Fang, P., Pandey, M.K., Murray, M.E., Kantarci, K., Jones, D.T., Vemuri, P., Graff-Radford, J., Schwarz, C.G., Machulda, M.M., Mielke, M.M., Roberts, R.O., Knopman, D.S., Petersen, R.C., Jack Jr., C.R., 2018. Widespread brain tau and its association with ageing, Braak stage and Alzheimer's dementia. Brain 141, 271–287.
Malone, I.B., Leung, K.K., Clegg, S., Barnes, J., Whitwell, J.L., Ashburner, J., Fox, N.C., Ridgway, G.R., 2015. Accurate automatic estimation of total intracranial volume: a nuisance variable with less nuisance. Neuroimage 104, 366–372.
Margulies, D.S., Vincent, J.L., Kelly, C., Lohmann, G., Uddin, L.Q., Biswal, B.B., Villringer, A., Castellanos, F.X., Milham, M.P., Petrides, M., 2009. Precuneus shares intrinsic functional architecture in humans and monkeys. Proc. Natl. Acad. Sci. U. S. A. 106, 20069–20074.
Marquie, M., Normandin, M.D., Vanderburg, C.R., Costantino, I.M., Bien, E.A., Rycyna, L.G., Klunk, W.E., Mathis, C.A., Ikonomovic, M.D., Debnath, M.L., Vasdev, N., Dickerson, B.C., Gomperts, S.N., Growdon, J.H., Johnson, K.A., Frosch, M.P., Hyman, B.T., Gomez-Isla, T., 2015. Validating novel tau positron emission tomography tracer [F-18]-AV-1451 (T807) on postmortem brain tissue. Ann. Neurol. 78, 787–800.
Mattsson, N., Ossenkoppele, R., Smith, R., Strandberg, O., Ohlsson, T., Jogi, J., Palmqvist, S., Stomrud, E., Hansson, O., 2018. Greater tau load and reduced cortical thickness in APOE epsilon4-negative Alzheimer's disease: a cohort study. Alzheimers Res. Ther. 10, 77.
McKhann, G.M., Knopman, D.S., Chertkow, H., Hyman, B.T., Jack Jr., C.R., Kawas, C.H., Klunk, W.E., Koroshetz, W.J., Manly, J.J., Mayeux, R., Mohs, R.C., Morris, J.C., Rossor, M.N., Scheltens, P., Carrillo, M.C., Thies, B., Weintraub, S., Phelps, C.H., 2011. The diagnosis of dementia due to Alzheimer's disease: recommendations from the National Institute on Aging-Alzheimer's Association workgroups on diagnostic guidelines for Alzheimer's disease. Alzheimers Dement. 7, 263–269.
Mechelli, A., Friston, K.J., Frackowiak, R.S., Price, C.J., 2005. Structural covariance in the human cortex. J. Neurosci. 25, 8303–8310.
Menkes-Caspi, N., Yamin, H.G., Kellner, V., Spires-Jones, T.L., Cohen, D., Stern, E.A., 2015. Pathological tau disrupts ongoing network activity. Neuron 85, 959–966.
Meyer-Luehmann, M., Coomaraswamy, J., Bolmont, T., Kaeser, S., Schaefer, C., Kilger, E., Neuenschwander, A., Abramowski, D., Frey, P., Jaton, A.L., Vigouret, J.M., Paganetti, P., Walsh, D.M., Mathews, P.M., Ghiso, J., Staufenbiel, M., Walker, L.C., Jucker, M., 2006. Exogenous induction of cerebral beta-amyloidogenesis is governed by agent and host. Science 313, 1781–1784.
Migliaccio, R., Agosta, F., Rascovsky, K., Karydas, A., Bonasera, S., Rabinovici, G.D., Miller, B.L., Gorno-Tempini, M.L., 2009. Clinical syndromes associated with posterior atrophy: early age at onset AD spectrum. Neurology 73, 1571–1578.
Minoshima, S., Frey, K.A., Foster, N.L., Kuhl, D.E., 1995. Preserved pontine glucose metabolism in Alzheimer disease: a reference region for functional brain image (PET) analysis. J. Comput. Assist. Tomogr. 19, 541–547.
Nelson, P.T., Alafuzoff, I., Bigio, E.H., Bouras, C., Braak, H., Cairns, N.J., Castellani, R.J., Crain, B.J., Davies, P., Del Tredici, K., Duyckaerts, C., Frosch, M.P., Haroutunian, V., Hof, P.R., Hulette, C.M., Hyman, B.T., Iwatsubo, T., Jellinger, K.A., Jicha, G.A.,

Kovari, E., Kukull, W.A., Leverenz, J.B., Love, S., Mackenzie, I.R., Mann, D.M., Masliah, E., McKee, A.C., Montine, T.J., Morris, J.C., Schneider, J.A., Sonnen, J.A., Thal, D.R., Trojanowski, J.Q., Troncoso, J.C., Wisniewski, T., Woltjer, R.L., Beach, T.G., 2012. Correlation of Alzheimer disease neuropathologic changes with cognitive status: a review of the literature. J. Neuropathol. Exp. Neurol. 71, 362–381.

Ossenkoppele, R., Zwan, M.D., Tolboom, N., van Assema, D.M., Adriaanse, S.F., Kloet, R.W., Boellaard, R., Windhorst, A.D., Barkhof, F., Lammertsma, A.A., Scheltens, P., van der Flier, W.M., van Berckel, B.N., 2012. Amyloid burden and metabolic function in early-onset Alzheimer's disease: parietal lobe involvement. Brain 135, 2115–2125.

Ossenkoppele, R., Cohn-Sheehy, B.I., La Joie, R., Vogel, J.W., Moller, C., Lehmann, M., van Berckel, B.N., Seeley, W.W., Pijnenburg, Y.A., Gorno-Tempini, M.L., Kramer, J.H., Barkhof, F., Rosen, H.J., van der Flier, W.M., Jagust, W.J., Miller, B.L., Scheltens, P., Rabinovici, G.D., 2015a. Atrophy patterns in early clinical stages across distinct phenotypes of Alzheimer's disease. Hum. Brain Mapp. 36, 4421–4437.

Ossenkoppele, R., Pijnenburg, Y.A., Perry, D.C., Cohn-Sheehy, B.I., Scheltens, N.M., Vogel, J.W., Kramer, J.H., van der Vlies, A.E., La Joie, R., Rosen, H.J., van der Flier, W.M., Grinberg, L.T., Rozemuller, A.J., Huang, E.J., van Berckel, B.N., Miller, B.L., Barkhof, F., Jagust, W.J., Scheltens, P., Seeley, W.W., Rabinovici, G.D., 2015b. The behavioural/dysexecutive variant of Alzheimer's disease: clinical, neuroimaging and pathological features. Brain 138, 2732–2749.

Ossenkoppele, R., Schonhaut, D.R., Baker, S.L., O'Neil, J.P., Janabi, M., Ghosh, P.M., Santos, M., Miller, Z.A., Bettcher, B.M., Gorno-Tempini, M.L., Miller, B.L., Jagust, W.J., Rabinovici, G.D., 2015c. Tau, amyloid, and hypometabolism in a patient with posterior cortical atrophy. Ann. Neurol. 77, 338–342.

Ossenkoppele, R., Schonhaut, D.R., Scholl, M., Lockhart, S.N., Ayakta, N., Baker, S.L., O'Neil, J.P., Janabi, M., Lazaris, A., Cantwell, A., Vogel, J., Santos, M., Miller, Z.A., Bettcher, B.M., Vossel, K.A., Kramer, J.H., Gorno-Tempini, M.L., Miller, B.L., Jagust, W.J., Rabinovici, G.D., 2016. Tau PET patterns mirror clinical and neuroanatomical variability in Alzheimer's disease. Brain 139, 1551–1567.

Ossenkoppele, R., Rabinovici, G.D., Smith, R., Cho, H., Scholl, M., Strandberg, O., Palmqvist, S., Mattsson, N., Janelidze, S., Santillo, A., Ohlsson, T., Jogi, J., Tsai, R., La Joie, R., Kramer, J., Boxer, A.L., Gorno-Tempini, M.L., Miller, B.L., Choi, J.Y., Ryu, Y.H., Lyoo, C.H., Hansson, O., 2018. Discriminative accuracy of [18F]flortaucipir positron emission tomography for Alzheimer disease vs other neurodegenerative disorders. JAMA 320, 1151–1162.

Peeraer, E., Bottelbergs, A., Van Kolen, K., Stancu, I.C., Vasconcelos, B., Mahieu, M., Duytschaever, H., Ver Donck, L., Torremans, A., Sluydts, E., Van Acker, N., Kemp, J.A., Mercken, M., Brunden, K.R., Trojanowski, J.Q., Dewachter, I., Lee, V.M., Moechars, D., 2015. Intracerebral injection of preformed synthetic tau fibrils initiates widespread tauopathy and neuronal loss in the brains of tau transgenic mice. Neurobiol. Dis. 73, 83–95.

Pontecorvo, M.J., Devous Sr., M.D., Navitsky, M., Lu, M., Salloway, S., Schaerf, F.W., Jennings, D., Arora, A.K., McGeehan, A., Lim, N.C., Xiong, H., Joshi, A.D., Siderowf, A., Mintun, M.A., investigators, F.A.-A, 2017. Relationships between flortaucipir PET tau binding and amyloid burden, clinical diagnosis, age and cognition. Brain 140, 748–763.

Prusiner, S.B., 1984. Some speculations about prions, amyloid, and Alzheimer's disease. N. Engl. J. Med. 310, 661–663.

Rabinovici, G.D., Furst, A.J., Alkalay, A., Racine, C.A., O'Neil, J.P., Janabi, M., Baker, S.L., Agarwal, N., Bonasera, S.J., Mormino, E.C., Weiner, M.W., Gorno-Tempini, M.L., Rosen, H.J., Miller, B.L., Jagust, W.J., 2010. Increased metabolic vulnerability in early-onset Alzheimer's disease is not related to amyloid burden. Brain 133, 512–528.

Raichle, M.E., 2011. The restless brain. Brain Connect 1, 3–12.

Raj, A., LoCastro, E., Kuceyeski, A., Tosun, D., Relkin, N., Weiner, M., For the Alzheimer's Disease Neuroimaging, I, 2015. Network diffusion model of progression predicts longitudinal patterns of atrophy and metabolism in Alzheimer's disease. Cell Rep. 10, 359–369.

Reijmer, Y.D., Schultz, A.P., Leemans, A., O'Sullivan, M.J., Gurol, M.E., Sperling, R., Greenberg, S.M., Viswanathan, A., Hedden, T., 2015. Decoupling of structural and functional brain connectivity in older adults with white matter hyperintensities. Neuroimage 117, 222–229.

Rosen, R.F., Fritz, J.J., Dooyema, J., Cintron, A.F., Hamaguchi, T., Lah, J.J., LeVine III, H., Jucker, M., Walker, L.C., 2012. Exogenous seeding of cerebral beta-amyloid deposition in betaAPP-transgenic rats. J. Neurochem. 120, 660–666.

Sander, K., Lashley, T., Gami, P., Gendron, T., Lythgoe, M.F., Rohrer, J.D., Schott, J.M., Revesz, T., Fox, N.C., Arstad, E., 2016. Characterization of tau positron emission tomography tracer [(18)F]AV-1451 binding to postmortem tissue in Alzheimer's disease, primary tauopathies, and other dementias. Alzheimers Dement. 12, 1116–1124.

Sanders, D.W., Kaufman, S.K., DeVos, S.L., Sharma, A.M., Mirbaha, H., Li, A., Barker, S.J., Foley, A.C., Thorpe, J.R., Serpell, L.C., Miller, T.M., Grinberg, L.T., Seeley, W.W., Diamond, M.I., 2014. Distinct tau prion strains propagate in cells and mice and define different tauopathies. Neuron 82, 1271–1288.

Scholl, M., Lockhart, S.N., Schonhaut, D.R., O'Neil, J.P., Janabi, M., Ossenkoppele, R., Baker, S.L., Vogel, J.W., Faria, J., Schwimmer, H.D., Rabinovici, G.D., Jagust, W.J., 2016. PET imaging of tau deposition in the aging human brain. Neuron 89, 971–982.

Scholl, M., Ossenkoppele, R., Strandberg, O., Palmqvist, S., Swedish Bio, F.s, Jogi, J., Ohlsson, T., Smith, R., Hansson, O., 2017. Distinct 18F-AV-1451 tau PET retention patterns in early- and late-onset Alzheimer's disease. Brain 140, 2286–2294.

Schroeter, M.L., Stein, T., Maslowski, N., Neumann, J., 2009. Neural correlates of Alzheimer's disease and mild cognitive impairment: a systematic and quantitative meta-analysis involving 1351 patients. Neuroimage 47, 1196–1206.

Schwarz, A.J., Yu, P., Miller, B.B., Shcherbinin, S., Dickson, J., Navitsky, M., Joshi, A.D., Devous Sr., M.D., Mintun, M.S., 2016. Regional profiles of the candidate tau PET ligand 18F-AV-1451 recapitulate key features of Braak histopathological stages. Brain 139, 1539–1550.

Seeley, W.W., Crawford, R.K., Zhou, J., Miller, B.L., Greicius, M.D., 2009. Neurodegenerative diseases target large-scale human brain networks. Neuron 62, 42–52.

Sepulcre, J., Sabuncu, M.R., Becker, A., Sperling, R., Johnson, K.A., 2013. In vivo characterization of the early states of the amyloid-beta network. Brain 136, 2239–2252.

Shirer, W.R., Ryali, S., Rykhlevskaia, E., Menon, V., Greicius, M.D., 2012. Decoding subject-driven cognitive states with whole-brain connectivity patterns. Cereb. Cortex 22, 158–165.

Smith, S.M., Fox, P.T., Miller, K.L., Glahn, D.C., Fox, P.M., Mackay, C.E., Filippini, N., Watkins, K.E., Toro, R., Laird, A.R., Beckmann, C.F., 2009. Correspondence of the brain's functional architecture during activation and rest. Proc. Natl. Acad. Sci. U. S. A. 106, 13040–13045.

Spires-Jones, T.L., Hyman, B.T., 2014. The intersection of amyloid beta and tau at synapses in Alzheimer's disease. Neuron 82, 756–771.

Tetzloff, K.A., Graff-Radford, J., Martin, P.R., Tosakulwong, N., Machulda, M.M., Duffy, J.R., Clark, H.M., Senjem, M.L., Schwarz, C.G., Spychalla, A.J., Drubach, D.A., Jack, C.R., Lowe, V.J., Josephs, K.A., Whitwell, J.L., 2018. Regional distribution, asymmetry, and clinical correlates of tau uptake on [18F]AV-1451 PET in atypical Alzheimer's disease. J. Alzheimers Dis. 62, 1713–1724.

Thal, D.R., Beach, T.G., Zanette, M., Heurling, K., Chakrabarty, A., Ismail, A., Smith, A.P., Buckley, C., 2015. [(18)F]flutemetamol amyloid positron emission tomography in preclinical and symptomatic Alzheimer's disease: specific detection of advanced phases of amyloid-beta pathology. Alzheimers Dement. 11, 975–985.

Villeneuve, S., Rabinovici, G.D., Cohn-Sheehy, B.I., Madison, C., Ayakta, N., Ghosh, P.M., La Joie, R., Arthur-Bentil, S.K., Vogel, J.W., Marks, S.M., Lehmann, M., Rosen, H.J., Reed, B., Olichney, J., Boxer, A.L., Miller, B.L., Borys, E., Jin, L.W., Huang, E.J., Grinberg, L.T., DeCarli, C., Seeley, W.W., Jagust, W., 2015. Existing Pittsburgh compound-B positron emission tomography thresholds are too high: statistical and pathological evaluation. Brain 138, 2020–2033.

Vlassenko, A.G., Vaishnavi, S.N., Couture, L., Sacco, D., Shannon, B.J., Mach, R.H., Morris, J.C., Raichle, M.E., Mintun, M.A., 2010. Spatial correlation between brain aerobic glycolysis and amyloid-beta (Abeta) deposition. Proc. Natl. Acad. Sci. U. S. A. 107, 17763–17767.

Vogel, J.W., Mattsson, N., Iturria-Medina, Y., Strandberg, O.T., Scholl, M., Dansereau, C., Villeneuve, S., van der Flier, W.M., Scheltens, P., Bellec, P., Evans, A.C., Hansson, O., Ossenkoppele, R., Alzheimer's Disease Neuroimaging, I, Swedish Bio, F.S, 2019. Data-driven approaches for tau-PET imaging biomarkers in Alzheimer's disease. Hum. Brain Mapp. 40, 638–651.

Walsh, D.M., Selkoe, D.J., 2016. A critical appraisal of the pathogenic protein spread hypothesis of neurodegeneration. Nat. Rev. Neurosci. 17, 251–260.

Wang, Z., Dai, Z., Gong, G., Zhou, C., He, Y., 2015. Understanding structural-functional relationships in the human brain: a large-scale network perspective. Neuroscientist 21, 290–305.

Whitwell, J.L., Graff-Radford, J., Tosakulwong, N., Weigand, S.D., Machulda, M., Senjem, M.L., Schwarz, C.G., Spychalla, A.J., Jones, D.T., Drubach, D.A., Knopman, D.S., Boeve, B.F., Ertekin-Taner, N., Petersen, R.C., Lowe, V.J., Jack Jr., C.R., Josephs, K.A., 2018. [(18) F]AV-1451 clustering of entorhinal and cortical uptake in Alzheimer's disease. Ann. Neurol. 83, 599–611.

Xia, M., Wang, J., He, Y., 2013. BrainNet viewer: a network visualization tool for human brain connectomics. PLoS One 8, e68910.

Yang, X., Beason-Held, L., Resnick, S.M., Landman, B.A., 2011. Biological parametric mapping with robust and non-parametric statistics. Neuroimage 57, 423–430.

Yeo, B.T., Krienen, F.M., Sepulcre, J., Sabuncu, M.R., Lashkari, D., Hollinshead, M., Roffman, J.L., Smoller, J.W., Zollei, L., Polimeni, J.R., Fischl, B., Liu, H., Buckner, R.L., 2011. The organization of the human cerebral cortex estimated by intrinsic functional connectivity. J. Neurophysiol. 106, 1125–1165.

Zhou, J., Gennatas, E.D., Kramer, J.H., Miller, B.L., Seeley, W.W., 2012. Predicting regional neurodegeneration from the healthy brain functional connectome. Neuron 73, 1216–1227.